The 1965 Mahavel Landslide (Réunion Island, Indian Ocean): Morphology, Volumes, Flow Dynamics, and Causes of a Rock Avalanche in Tropical Setting

Laurent Michon, Eric Gayer, Antoine Lucas, Franziska Bellin, Matthieu Gougeon

The 1965 Mahavel Landslide (Réunion Island, Indian Ocean): Morphology, Volumes, Flow Dynamics, and Causes of a Rock Avalanche in Tropical Setting

Laurent Michon[1,2] , Eric Gayer[2], Antoine Lucas[2] , Franziska Bellin[1], and Matthieu Gougeon[2]

[1]Université de La Réunion, Laboratoire GéoSciences Réunion, Saint Denis, France, [2]Université Paris Cité, Institut de physique du globe de Paris, CNRS, Paris, France

Abstract In May 1965, a main landslide occurred in a deeply incised valley of Piton de la Fournaise volcano, in Réunion Island. This event occurred one day after heavy rainfalls and was consequently interpreted as a mud/debris flow. We take advantage of several sets of historical photographs to reappraise this event. They show that the collapse of a large part of the valley headwall produced a rock flow that dropped 1,740 m and traveled 5,050 m. The surface morphology suggests that the landslide produced a main flow that evolved in a secondary flow in the distal part. The main flow deposit is composed of a matrix-rich fragmented facies and a jigsaw-fracturated facies. The matrix presents a gravely-to-silty granulometry and fractal dimensions ranging between 2.472 and 2.865. Volumes of the collapsed material (59.7 ± 3.1 Mm^3) and the deposit (46 ± 13 Mm^3) were determined from a photogrammetric approach. We estimated velocities ranging between 86 and 44 m s^{-1} along the flow path. Our simulations with SHALTOP reveal that the landslide geometry and velocities are well reproduced with frictional Coulomb rheology. We thus interpret the 1965 Mahavel landslide as a main rock avalanche rather than a mud/debris flow. We propose that the trigger of the 1965 avalanche, and of the smaller events in 1995 and 2001, is the water infiltration related to the intense rainfalls, which systematically preceded by one day each collapse. Finally, the succession of dry and wet years before each collapse event could promote favorable conditions to failure.

Plain Language Summary In 1965, a main landslide occurred in a deeply incised valley of Réunion Island (Indian Ocean). It followed heavy rainfalls and was consequently interpreted as a main mudflow. We used historical photographs, deposit descriptions, and numerical simulations to reappraise this event that fortunately did not have any casualties. We show that about 60 Mm^3 of volcanic rocks suddenly collapsed and produced a rock avalanche that traveled over a total distance of 5 km. The flow traveled at velocities ranging between 86 and 44 m s^{-1}. We interpret this landslide as a rock avalanche instead of a mudflow. Our work finally suggests that the annual precipitation variability could be a main conditioning factor that promotes scarp collapses and consequently enhances erosion. The increase of precipitation variability with climate warming could therefore increase the occurrence of large collapses and rock avalanches in mountainous areas.

1. Introduction

Rock avalanches are devastating geological processes and one of the most threatening natural hazards due to the large volume of rocks involved (frequently >10 Mm^3), their long runout and their high velocity (e.g., Dufresne et al., 2016; Evans, 2006; Hungr et al., 2014; Legros, 2002; Lucas et al., 2014; Perinotto et al., 2015). They develop in mountainous areas where the triggers can be a sudden change in the ambient geophysical stresses (i.e., earthquakes or volcanic eruptions; e.g., Evans, Roberts, et al., 2009; Weidinger et al., 2002; Xing et al., 2017) and/or of the hydrometeorological conditions (e.g., Costa, 1991; Crosta et al., 2004; Martha et al., 2015). Extreme rain conditions preceded by a few days the two largest historical landslides of Réunion Island, where long-term erosion rates are among the highest on Earth (Gayer et al., 2019; Salvany et al., 2012). On 26 November 1875, part of the northern scarp of Piton des Neiges volcano summit collapsed after several days of heavy rains (de Cordemoy, 1876), producing a landslide of about 20 Mm^3 that killed 62 people in the Salazie topographic depression (Figure 1a; Bret, Fèvre, et al., 2003). Almost 100 years later, on 6 May 1965, the eastern scarp of a tributary (Bras de Mahavel) of the Rivière des Remparts suddenly collapsed also after intense rainfalls (see Section 2.2 for details). In consequence, this event was interpreted as a large mud/debris

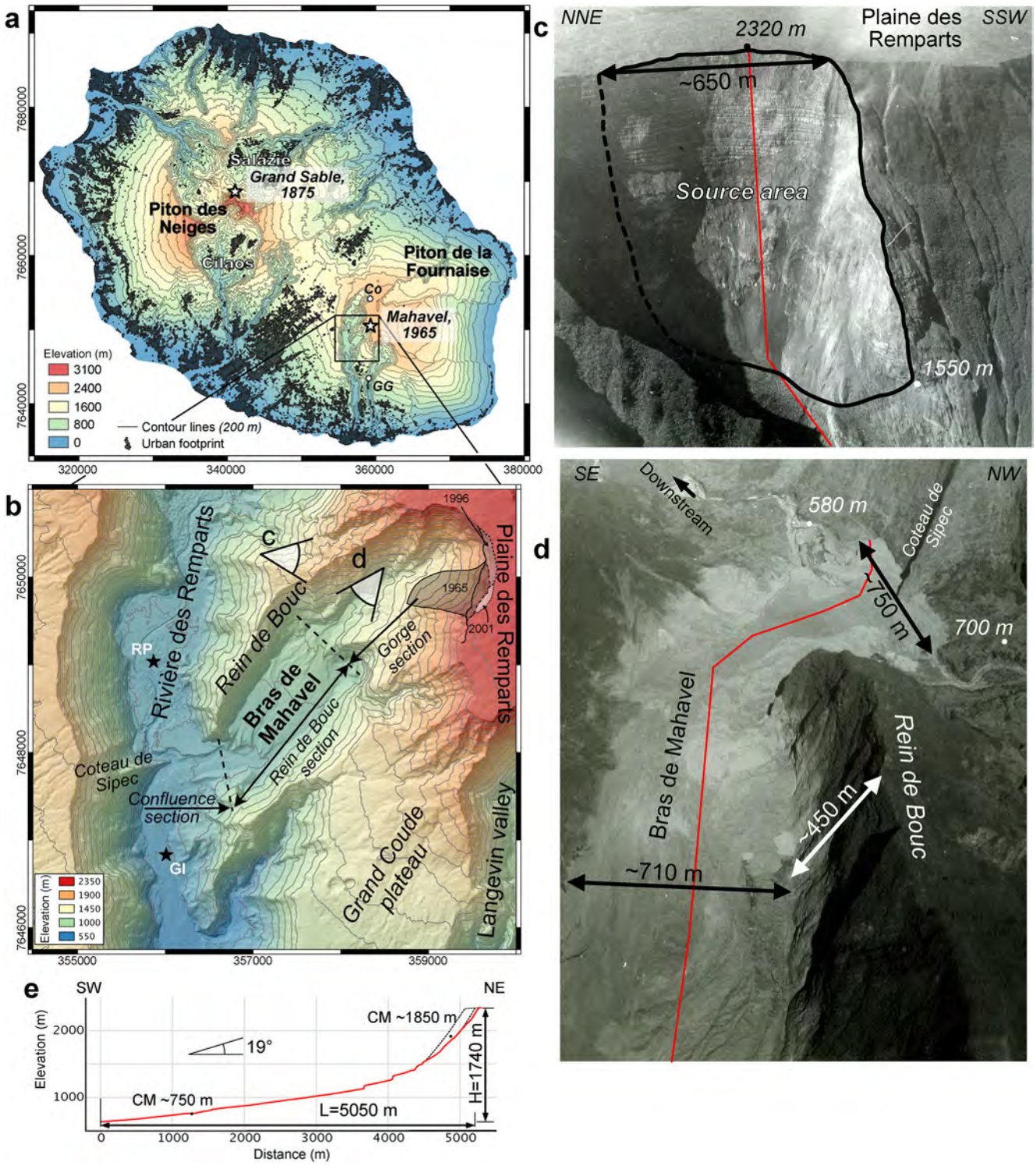

Figure 1.

flow (BRGM, 1965) or a debris avalanche rapidly evolving in debris flows or lahar (Merle et al., 2008). This event that occurred during night time fortunately did not reach the hamlets located upstream and downstream of the confluence between the Bras de Mahavel and Rivière des Remparts and, consequently, had no immediate human impacts.

This work aims at assessing the dynamics of landslides (mud/debris flow or rock avalanches) related to scarp collapses with a special focus on the event of Mahavel in 1965. First, we used historical aerial photographs taken in 1965 and 1966 to identify the source area and the flow path and map the deposit. Second, we described the deposit sedimentary facies and granulometry. Third, we quantified the volumes of collapsed material and landslide deposit from digital elevation model (DEM) computed from aerial photographs of the French national geographic institute (IGN) taken in 1961 and 1966, that is, before and after the landslide, respectively. Finally, we constrained the flow dynamics using the frontal and lateral runup elevations, the center of mass displacement and numerical simulations and conclude that the 1965 Mahavel landslide produced a rock avalanche rather than the proposed mud/debris flow (BRGM, 1965; Merle et al., 2008).

2. General Background

2.1. Geological Setting

Réunion Island is the subaerial part of a ~7,000 m high volcanic edifice, lying at ~4,000 m on the ocean floor, located 700 km east of Madagascar, and related to the Réunion hotspot (Richards et al., 1989). The magma emission, since around 2 Ma in subaerial domain (McDougall, 1971), led to the multi-stage building of two basaltic volcanoes (Gayer et al., 2021; Gillot et al., 1994; Salvany et al., 2012). Both volcanic edifices, Piton des Neiges in the west and Piton de la Fournaise in the east (Figure 1a), are composed of hundred to thousand meters thick piles of lava flows accumulated during the periods of volcanic activity, intercalated with breccia units related to the volcanoes dismantling during periods of quiescence (Bret, Fèvre, et al., 2003; Chaput et al., 2017; Merle et al., 2010).

Réunion Island presents a mountainous morphology made of deeply incised watersheds that cut the Piton des Neiges dormant volcano (3,000 m above sea level, asl) and the western part of Piton de la Fournaise whose elevation reaches more than 2,500 m asl (Figure 1a). This dissected landscape results from an intense edifice erosion initiated around 60–70 ka after the last building period of Piton des Neiges and the eastward migration of the Piton de la Fournaise eruptive center (Gayer et al., 2019, 2021; Mairine & Bachèlery, 1997). The deeply incised valleys are limited by scarps of 700–1600 m in height and average slopes >50°. They show a geometry that evolves from narrow canyons in their downstream sections to enlarged subcircular topographic depressions upstream, called cirques, or to a network of coalescent tributaries.

The Rivière des Remparts valley corresponds to the second group of geometry, with a deep canyon that is enlarging upstream due to the connection of tributaries flowing southwestward from the Plaine des Remparts plateau (Figure 1b). The atypical orientation of the Rivière des Remparts canyon, almost concentric instead of radial to the volcano's summit, is comparable to that of the Waimea canyon in Kauai (Hawaii) or the drainage system on the northern and southern flanks of Tahiti-Nui (French Polynesia). In both cases, erosion was controlled by main tectonic discontinuities such as landslide scars (Duffield et al., 1982; Hildenbrand et al., 2008; Sherrod et al., 2021). One of the tributaries of the Rivière des Remparts, named Bras de Mahavel, has its highest and lowest elevations at 2320 m asl and 600 m asl, respectively (Figure 1b). This canyon, 4 km in length, is bounded on the right and left banks by the Rein de Bouc scarp and the Grand Coude plateau. It presents three different sections. The upstream segment, here called the gorge section, is characterized by a 1 km long, 700–900 m deep gorge whose floor is ~50 m wide. The intermediate segment, named the Rein de Bouc section, is 1.8 km long and is characterized by a valley floor that is abruptly enlarged to 700–750 m at the end of the gorge section and narrows downstream to 400 m. Note that the gorge and Rein de Bouc sections account for the C1 and C2 compartments of Garcin et al. (2005). Finally, the confluence section, not defined by the latters, corresponds to the connection between the Bras de Mahavel tributary with the Rivière des Remparts valley that flows from north to south. The headwall of the Bras de Mahavel canyon, which collapsed during the 1965 landslide, is made of a 500 m thick succession of westward dipping reddish scoria layers and interbedded lava flows in tectonic contact

Figure 1. (a) Morphology of Réunion Island showing the deeply incised valleys in the volcanic massif of Piton des Neiges and Piton de la Fournaise. The two largest rapid landslides (the Grand Sable and Mahavel events) are indicated by white stars. The urban footprint (from www.peigeo re) reveals that similar events would have major impacts in the depressions of Cilaos and Salazie. White dots account for the Commerson (Co) and Grand Galet (GG) gauge stations used in Figure 3, Figures S1 and S5 in Supporting Information S1. (b) Morphology of the Bras de Mahavel canyon. This 4-km long NE-SW valley is a tributary of the Rivière des Remparts canyon. The former presents a U-shaped headwall, the gorge, Rein de Bouc and confluence sections. Black stars account for the Grande Ilet (GI) and Roche Plate (RP) hamlets. The footprints of the 1996 and 2001 collapses discussed in Section 5 are indicated for information. The 1965 Mahavel landslide resulted from the collapse of part of the Plaine des Remparts (c) and flew in the Bras de Mahavel tributary down to the Rivière des Remparts valley floor (d). Coordinates in meter, WGS 84/UTM zone 40S. (e) Longitudinal profile along the Mahavel canyon covered by the avalanche deposit represented in (c and d). Total vertical drop (H) and horizontal displacement (L) of the avalanche suggest a fahrböschung of 19° and an H/L of 0.344. CM accounts for the elevations of the center of mass of the fallen mass and deposit.

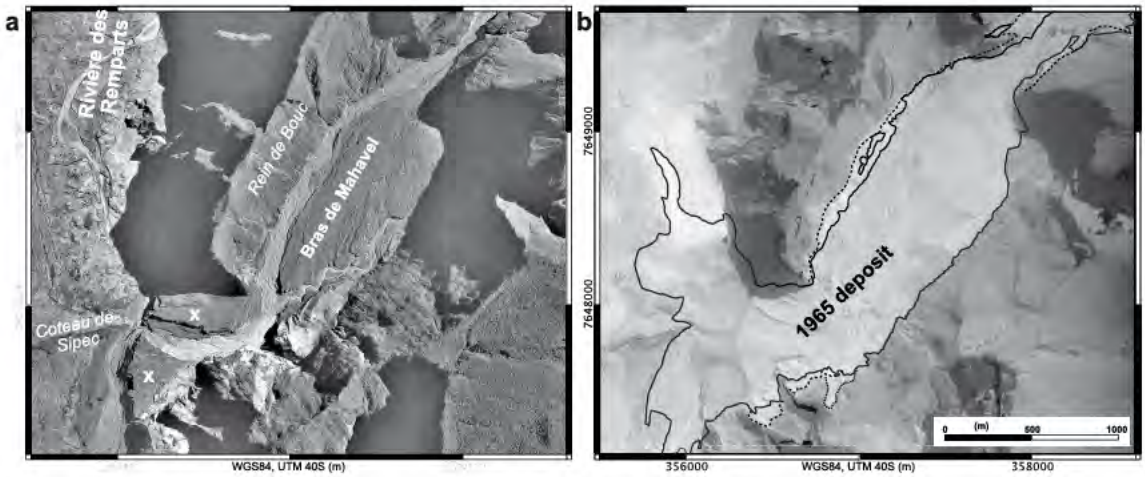

Figure 2. Orthoimages of 1950 (a) and 1966 (b), that is, before and after the 1965 rock avalanche. The orthophotography of 1950 is provided by the French national institute of geography (IGN), while we computed that of 1966 from historical aerial photographs of IGN with the photogrammetry procedure detailed in Lucas and Gayer (2022). The X in (a) accounts for main terraces formed by previous, yet undated, main sediment inputs.

with a 300 m thick pile of massive gray horizontal 'a'ā lava flows older than 60 ka in the upper part (Merle et al., 2008). The fault separating the two units corresponds to the outer limit of the Morne Langevin caldera that formed around 150 Kyrs ago (Figure 2; (Bachèlery & Mairine, 1990; Merle et al., 2008, 2010).

Before 1965, the floor of the Rein de Bouc section of Bras de Mahavel was drained by a 40–100 m wide linear dry channel located at the base of Rein de Bouc and a small sinuous river fed by several springs located in the eastern scarp (Figure 2a). Both systems merge in an E-W channel that flows between two large terraces in the confluence section.

2.2. Meteorological Setting

The climate of Réunion Island is tropical and the precipitation distribution is strongly influenced by the interaction between the westward trade winds and the high volcanic reliefs (Réchou et al., 2019 and references therein). In the area of the Rivière des Remparts valley, the 1969–2001 mean annual precipitation recorded at the Grand Galet (in the Langevin adjacent valley) and Commerson gauge stations (Figure 3a, see Figure 1a for location) reach 3,160 and 3,820 mm, that is, around the catchment central and upper parts. Moreover, the island's climate is characterized by a rainy season in summer, from November to April, and a drier one in winter, between May and October. Beside a mean annual rainfall amount ~20% greater at the catchment highest elevations than in its central part, the Commerson gauge station records a mean cumulative summer precipitations 60% larger than at Grand Galet station (Figure 3a). This difference is due to the increasing amount of precipitation with altitude in summer while the atmospheric thermal inversion layer is frequently lacking (Figure 3a; Barcelo & Coudray, 1996; Gayer et al., 2019; Réchou et al., 2019). Conversely, the presence of the thermal inversion layer in winter yields a mean rain deficit of 47% of the catchment upper part compare to the valley central part (Figure 3a).

Before 1968, our knowledge of the rainfall distribution in the area of the Rivière des Remparts was limited to the Grand Galet rain gauge located in the central part of the adjacent Langevin valley (Figure 1b). At a pluri-annual time scale, the rainfall record shows that the 1965 avalanche was preceded by two abnormally wet years (1964–1965) following three particularly dry years (1961–1963; Figure 3b; Figure S1 in Supporting Information S1). At a shorter time scale, the 1965 Mahavel avalanche occurred one day after a discrete event (May 2 to 4) of intense rainfalls (around 240 mm) related to the Rose tropical storm (Figure 3c). More remarkably, this event shortly followed a larger one during which almost 800 mm accumulated between 17 and 22 April 1965.

3. Data and Methods

3.1. Photos, Maps, and Digital Elevation Models

The landslide occurred in a remote place over the night and was therefore not directly witnessed. Consequently, we use several sets of contemporary photographs to characterize the dynamics of the 1965 Mahavel landslide. We

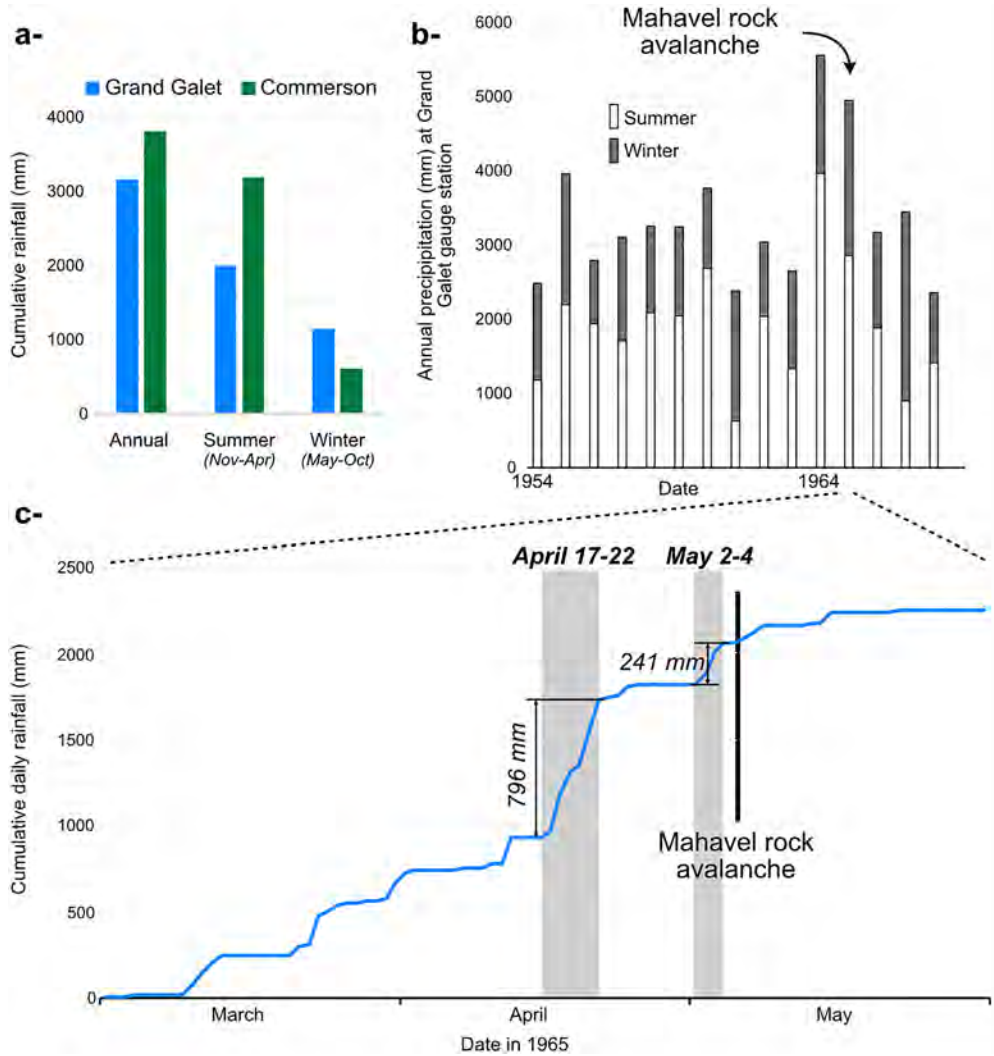

Figure 3. (a) Mean annual, summer and winter precipitations recorded at Grand Galet and Commerson gauge stations between 1969 and 2001 (data Météo France, 2023). At Réunion Island, the summer corresponds to the rainy season that lasts from November to the end of April. Winter is from May to October. (b) Precipitations recorded at Grande Galet gauge station between November 1953 and October 1968, the only station that continuously recorded precipitations close to the Mahavel canyon at that time (see Figure 1a for location; Meteo France, 2023). Each year *n* is subdivided in a rainy season from November *n*-1 to April *n* (white bars) and a drier season between May and October (dark gray bars). The black dashed line accounts for the mean annual precipitation. (c) Rainfalls recorded between March and May 1965 at the Grand Galet gauge station. Two heavy rainfall events (gray bars) preceded the Mahavel avalanche.

first use pictures taken during two low-level flights after the event by J. Legros. The first flight was likely made a few days after the collapse, as suggested by the dust clouds due to rockfalls in the still unstable collapse zone. This data set allows us to map the deposits and to characterize its morphology. The second flight was probably performed a few months after the landslide since the pictures show a significant remobilization of the deposit. Both sets of pictures enable us to reconstruct the chain of events from the collapse to the remobilization of the deposit.

The second set of photographs corresponds to stereoscopic aerial pictures made by the French Geographic Institute (IGN) in August/September 1961 and April/September 1966, that is, around 4 years before and 1 year after the landslide, respectively. DEMs of both dates are generated following the photogrammetric method of Lucas and Gayer (2022). We reconstruct elevation grids of the area, from sensor calibration and dense matching of the historical aerial images. We produce DEMs with a spatial resolution of 1.25 m and orthoimages for both dates (see Figure S2 in Supporting Information S1 for the orthoimages of 1961 and 1966). Differences of DEM are

used to estimate the change in elevation on the scar and the deposit areas and to calculate the failed volume and the volume of deposit, respectively. Errors on the volumes are estimated from the errors on the differences of DEMs, which are estimated from differences in elevation on stable areas (with no geomorphic change). Seventeen stable areas (with no geomorphic changes), located on the stable flanks of the Piton de la Fournaise volcano and around Rivière des Remparts, show an average difference in elevation of 0.018 m between 1961 and 1966. Such a small difference demonstrates that the two DEMs (1961 and 1966) are very well aligned (horizontally and vertically) with no offset between them. This also shows that the grids do not suffer from radial distortion. However, the standard deviation of 3.2 m for the differences on the 17 stable areas reveals some expected dispersion that is mainly due to the lack of any post-correlation regularization (in order to keep the signal as raw as possible) and to dense vegetation on the stable flanks, which complicates the correlation between images. Finally, errors on the failed volume and the volume of deposits were estimated using a 95% confidence level on the differences of stable areas, that is, 6.4 m.

3.2. Grain Size Distribution

A grain size analysis was conducted on seven samples taken from homogeneous facies of the 1965 Mahavel deposit. A portion of the matrix component (<50 mm) of each sample was dried and sieved between 16 mm and 40 μm with a vibrating table for 10 min. Using the resulting grain size distribution of each sample and a volcanic product density of 2.9 and, we estimated the number of grains for each sieve interval. Plots of the data (grain size vs. number of particles) allowed to determine the sample fractal dimension that is the scaling exponent in the power-law relationship (Hooke & Iverson, 1995).

3.3. Landslide Dynamics

In this study, we determine the landslide dynamics using two complementary methods. We calculate first ranges of landslide velocities (a) from empirical laws (Chow, 1959; McClung, 2001; Prochaska et al., 2008; Scheidl et al., 2015) applied to the frontal and lateral runups observed along the flow path and (b) from the height difference between the estimated centers of mass of the collapsed material and the deposit (Ekström & Stark, 2013; Yamada et al., 2018). Second, we perform simulations of the flow with the SHALTOP model (Bouchut et al., 2003; Mangeney-Castelnau et al., 2005) where the Saint-Venant equations are generalized to an arbitrary 2D topography scalar field accounting for its second derivative (i.e., the curvature terms) after Bouchut and Westdickenberg (2004). The interaction between the flow and the bottom topography is expressed through a basal stress, which is depth-integrated (Bouchut et al., 2003). This model has been validated on analytical solution (Lucas et al., 2007), experimental results (Lucas et al., 2007; Mangeney-Castelnau et al., 2005; Mangeney et al., 2007), as well as numerous natural cases under wide geological and climatic conditions (e.g., Hibert et al., 2011; Lucas & Mangeney, 2007; Lucas et al., 2007, 2011, 2014; Moretti et al., 2015).

In this study, back-analysis shows that a purely frictional Coulomb rheology provides a good agreement with observations on both velocity and runout distance (e.g., Ancey & Meunier, 2004; Favreau et al., 2010; Lucas et al., 2007). Note that other rheologies require more advanced back-analysis as they depend on more parameters, mostly empirical (e.g., Lucas et al., 2007, 2014; Mangeney et al., 2007).

The bottom topography is obtained from the 1961 DEM from which we have subtracted the equivalent volume to the upstream scarp, itself obtained from the difference between the 1966 and 1961 DEMs. The initial mass is obtained from the difference between the 1961 DEM and this bottom topography. A vertical offset of 43 m is then applied to reduce the initial mass volume in order to fit the final deposits volume (46 Mm^3, see Section 4.2) while keeping the same slopes of the initial mass as to keep the same pressure forces at the initial stage of the simulation.

4. Results

4.1. Deposit Characteristics

On 6 May 1965 1 day after the heavy precipitations (Figure 3c), the upper scarp of the Bras de Mahavel tributary collapsed. Aerial photographs taken shortly after the collapse reveal a huge scar in the scarp having a height of around 900 m, a width of around 650 m and a lateral cliff retreat of the Plaine des Remparts of 150 m (Figure 1). The landslide deposit outcrops in the gorge section covered the 700-m-wide Bras de Mahavel valley floor of the Rein de Bouc section and spread on the Rivière des Remparts floor in the confluence section (Figure 4).

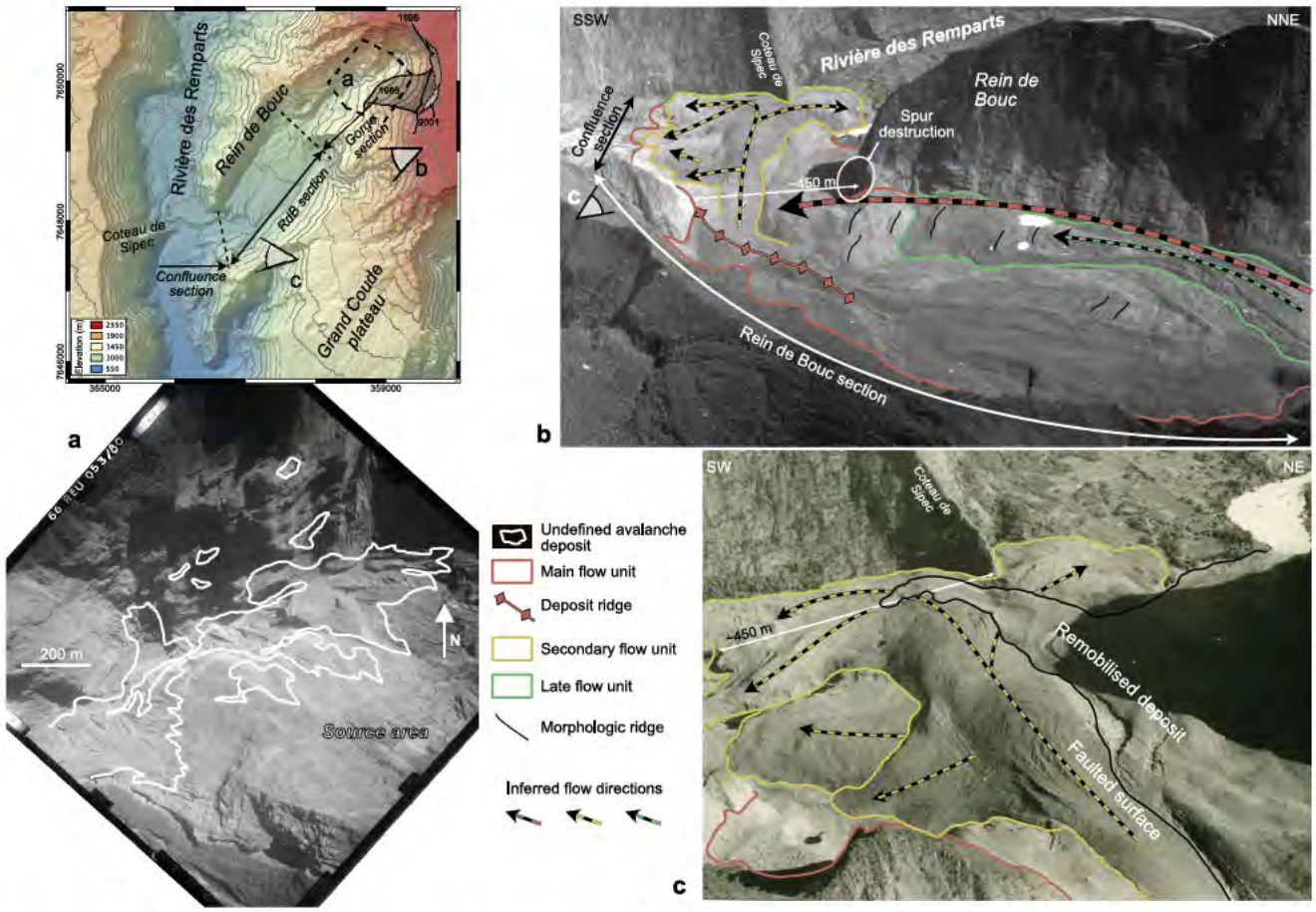

Figure 4. 1965 Mahavel landslide deposit in the gorge (a), Rein de Bouc (b) and confluence (b, c) sections. The surface morphology and geometric relationships allow to identify a basal main flow unit (red contours), a secondary flow (yellow contours) connected to the main zone of deposit accumulation where a deposit ridge remains, and a third final unit located at the base of the Rein de Bouc valley flank (green contours). See text for description. Photos: J. Legros. RdB: Rein de Bouc. Coordinates in meter, WGS 84/UTM zone 40S.

The flow traveled over a total distance of 5,050 m until the base of Coteau de Sipec in the Rivière des Remparts (Figures 1d, 1e, and 4). The highest part of the collapse area lying at 2,320 m above sea level (asl) and the lowest elevation of the landslide deposit being at 580 m asl, the total vertical drop H is of 1,740 m, the H/L ratio is 0.344 and the fahrböschung is of 19° (Figure 1e).

The analysis of the aerial photographs of J. Legros reveal that a small part of the deposit accumulated in the gorge section after the collapse of the headwall scarp. Considering its distribution that is partially visible on a few pictures, a volume of 4–5 Mm^3 concentrated at the base of the scar can be inferred. Noteworthily, the IGN pictures taken in April 1966 show that most of this deposit on the gorge floor was already remobilized one year after the avalanche (Figure 4a). These photos also show deposits perched on the northwest scarp, 300 m above the valley floor, suggesting extreme dynamics related to the collapse of the valley headwall.

In the Rein de Bouc and confluence sections, the photographs enable us to identify three flow units that differ in terms of surface morphology, spatial extent, and timing (Figure 4). The largest, main flow unit forms an apron on the valley floor of the Rein de Bouc and confluence sections. It is overlapped by a narrow, late unit restricted to the foot of the Rein de Bouc valley flank, and, downstream, by a secondary flow originating at the base of a main ridge formed by the deposit of the main unit (Figure 4b). Both main and late flow units present a chaotic morphology with morphologic ridges and lows perpendicular to the valley axis. Note that only the late flow shows levées surrounding flow channels. This surface morphology strongly contrasts with that of the secondary unit, which presents a densely faulted surface, especially on the main E-W axis that is diverging in spreading tongues flowing upstream and downstream in the Rivière des Remparts valley floor (Figure 4c). Despite a large difference of the flow size, the secondary flow presents structures very similar to those observed on the distal lobe of the Socompa avalanche (Kelfoun et al., 2008).

Whatever the units, the aerial photographs of J. Legros and IGN do not show any hummocks at the deposit surface in the Rein de Bouc and confluence sections. This observation is consistent with the lack of large blocks (long axis of >10 m) at the surface of the deposit (BRGM, 1965). Since 1965, river incision cut the avalanche deposit over a maximum thickness of ∼70 m on the Bras de Mahavel left bank (Figure 5a). In the right bank, where outcrops are more accessible, the deposit exposures reveal the main flow unit internal texture over a thickness of ∼10 m (Figure 5b). From top to base, the avalanche body is made of two facies that present similarities with the jigsaw-fracturated facies and the fragmented facies of Dufresne et al. (2016). The former is characterized by abundant coarse angular to very angular light gray clasts of massive basalt up to centimeter to several decimeters in size. They are either concentrated in discontinuous meter-thick levels presenting an elongated organization or isolated blocks in a brownish-red matrix whose color is similar to the scoria-rich units at the base of the Bras de Mahavel headwall scarp (Figure 5b). The size of sheared fragmented blocks may strongly vary and be decametric like at Mount Meager (Roberti et al., 2017). The matrix around the fracturated blocks is composed of 76%, 22%, and 2% of gravels, sands and silts, respectively (sample MAH17-1 in Figure 6).

The matrix-rich fragmented facies, brown in color, presents a much finer granulometry with scattered survivor angular basaltic clasts rarely exceeding 10 cm (Figure 6). The grain size distribution of the matrix reveals a lower amount of gravels (46%–54%) than in the jigsaw-fracturated facies and conversely a higher proportion of silts (3%–12%; Figure 6). This part of the avalanche deposit also presents extremely fragmented and sheared blocks identified from their color and showing a boudinage geometry (Figure 6c).

Fractal dimensions determined from the grain size distribution range from 2.472 in the jigsaw-fracturated facies to 2.742–2.865 in the matrix-rich fragmented one (mean value of 2.77; Figure 6c). These values of fractal dimension that are in the range commonly determined for rock avalanches (e.g., Crosta et al., 2007; Dufresne & Dunning, 2017) suggest a stronger fragmentation in the matrix-rich fragmented facies than in the jigsaw fracturated facies.

4.2. Volume Estimates

The deficit elevation in the collapsed area, the thickness of the deposit, and the volumes of the collapsed pile of rock and of the landslide deposit are determined from the DEMs reconstructing the topography of the valley of Bras de Mahavel using the stereoscopic images of 1961 and 1966 and the workflow described in Lucas and Gayer (2022) (Figure 7; Figure S2 in Supporting Information S1). Figure 7b indicates that most of the volume of the source area originates from two sectors where the elevation deficit exceeds 200 m. They correspond to the central part of the scar and an E-W topographic ridge that almost entirely collapsed. It indicates that the avalanche was mainly composed of (a) the horizontal 'a'ā lava flows observed in the upper part of the scarp and (b) the westward dipping scoria layers forming the topographic ridge. Downstream, the landslide deposit filled the channels incised in the pre-1965 deposits, especially in the confluence section where it reaches a maximum thickness of more than 100 m (Figure 7c). Noteworthily, the thick deposit accumulations in this section, that is, in the E-W pre-existing channel and on both sides of Coteau de Sipec, result from the secondary flow unit, as suggested by the aerial photographs taken shortly after the collapse event (Figures 4b and 4c).

The volumes of the displaced material quantified from the difference of DEM (DOD) correspond to 59.7 ± 3.1 Mm^3 and 46 ± 13 Mm^3 for the collapsed pile of rock and the landslide deposit, respectively. Nevertheless, the errors on the surface reconstruction depend strongly on the slope of the topography. Thus, due to a slope >70°, we suspect and consider that the uncertainties on the volume of the collapsed cliff must be larger than those we indicate, without being able to estimate it precisely. Note that the volume of the landslide deposits agrees well with the two volumes of the deposit already proposed (50 Mm^3 by BRGM (1965) with undisclosed method and 48 Mm^3 by PGRI (2009) with difference between IGN topographic maps). Yet, the volume of the initial mass has never been calculated and therefore, our volume cannot be compared to other estimation methods.

4.3. Flow Path and Chain of Events

Despite a lack of any direct observation of the scarp collapse and the landslide, the different sets of aerial photographs allows to determine the overall flow path and the chain of events that occurred in the Bras de Mahavel tributary (Figure 8).

Although the Bras de Mahavel valley is a rather linear NE-SW trending structure, the location of the detached cliff on the southern headwall of the valley led to an overall curved flow path bended toward the north (Figure 8). The trimline, which corresponds to the upper bound of the flow, is extremely well defined by the damaged vegetation

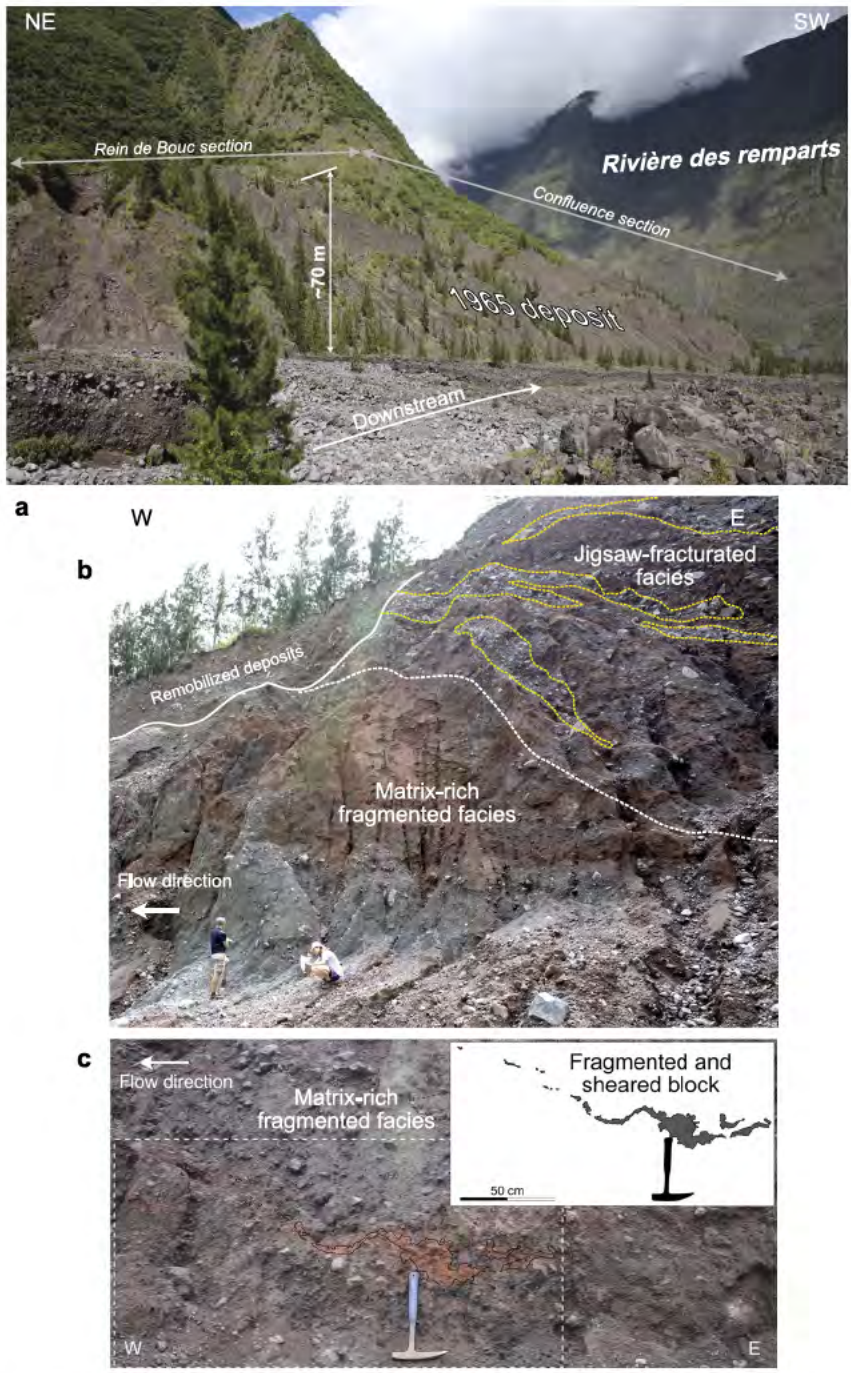

Figure 5. (a) Remaining deposit of the 1965 Mahavel avalanche in the left bank of the Bras de Mahavel tributary. The deposit still forms a ~70-m-high topographic ridge. (b) Avalanche deposit of the main flow unit in the right bank downstream of the Rein de Bouc disintegrated spur. The deposit presents a matrix-rich fragmented facies in the scarp lower half and a jigsaw-fracturated facies in the upper part of the deposit exposure. Yellow dashed lines delineate fracturated elongated blocks. (c) Intensely fragmented and sheared blocks with the matrix-rich fragmented facies. Note the severe shearing of the red block isolated in the panel on the figure upper right corner.

on the valley flanks (Figure S3 in Supporting Information S1). It allows us to estimate the runups and the flow path along the Bras de Mahavel valley. The photo data set suggests that part of the debris stream flowed northwestward and ran up on the opposite side of the collapsed cliff where it stripped the vegetation over 300–380 m above the canyon floor (stage 1 in Figures 8a–8c). Probably in the meantime, the main part of the rock stream moved westward and was laterally confined between the cliff of the Cap des Oiseaux Verts and the steep southern bank. There,

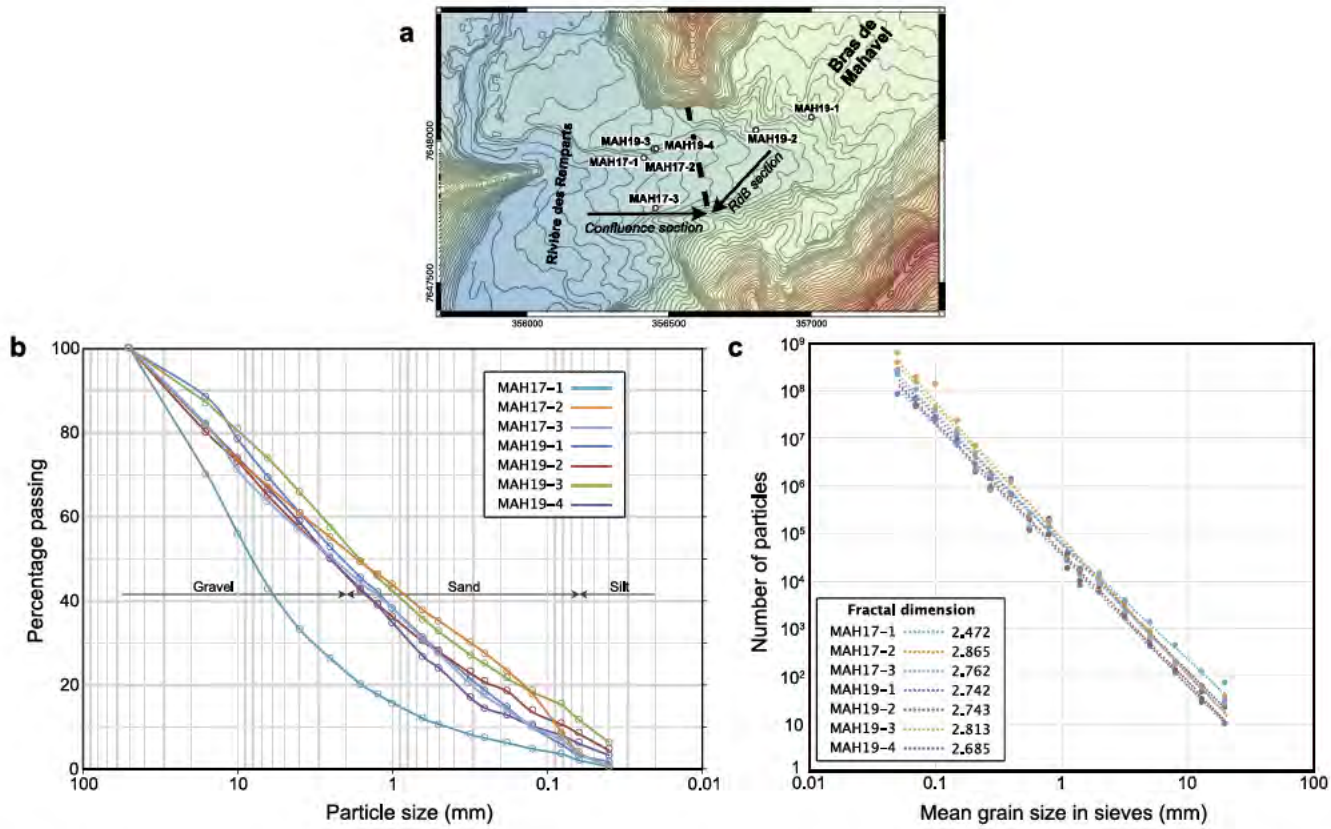

Figure 6. (a) Sample location of the 1965 Mahavel avalanche deposit. (b) Grain size distribution of bulk matrix samples (<50 mm). (c) Grain size versus number of particles for the samples of the 1965 avalanche deposit. Fractal dimensions have been determined using the technique of Hooke and Iverson (1995). For the set of samples, the lines of best fit from the fractal dimension is deduced provide r^2 between 0.991 and 0.997.

the flow reached 170–190 m on both sides of the valley and then entered the Rein de Bouc section (Figure S3a in Supporting Information S1). The sharp trimline, on the sole northern scarp of the valley (i.e., the Rein de Bouc), indicates an asymmetric superelevation of the debris stream on the north flank of the valley over 100–150 m above the pre-collapsed valley floor (stage 2 in Figures 8b and 8d; Figure S3b in Supporting Information S1). The undulated geometry of the trimline on the Rein de Bouc scarp indicates extremely turbulent flow dynamics (Figure 8d). Then, the debris stream, laterally constrained by the northern bank, crossed back the valley to the southern wall and caused on the way the disintegration of the 150 m high and 100 m wide spur of the Rein de Bouc (stage 3 in Figures 8b, 8d and 8e). In the southern wall, the final runup was limited to 100 m above the pre-landslide valley floor but the flow locally damaged the vegetation over 300 m high on the southern valley scarp (stage 4 in Figures 8b and 8e). At this point, the flow was deflected westward and spread in the Rivière des Remparts main trunk. The lack of any trimline and dust on the western bank of Rivière des Remparts suggests that the flow slowly stalled upstream and downstream of Coteau de Sipec, on the valley floor (stage 5 in Figures 8b and 8d). This observation agrees with the faulted surface of the deposit that indicates a slow spreading. The deposit eventually dammed the valley floor and led to the development of two temporary lakes in the Bras de Mahavel and the Rivière des Remparts (Figure 9a).

Finally, the landslide deposit was partially remobilized during subsequent heavy rainfalls, producing debris flows that mainly accumulated in the downstream section of Rein de Bouc and upstream of the landslide deposits in the Rivière des Remparts, and covered the landslide primary deposit (Figure 9).

4.4. Back Analysis on Landslide Dynamics

4.4.1. Analytical Calculations

The Mahavel landslide destroyed vegetation on the valley scarps that allows us to determine frontal and lateral runups and therefore assess the flow velocity on several sites. In the gorge section, the flow ran up the canyon

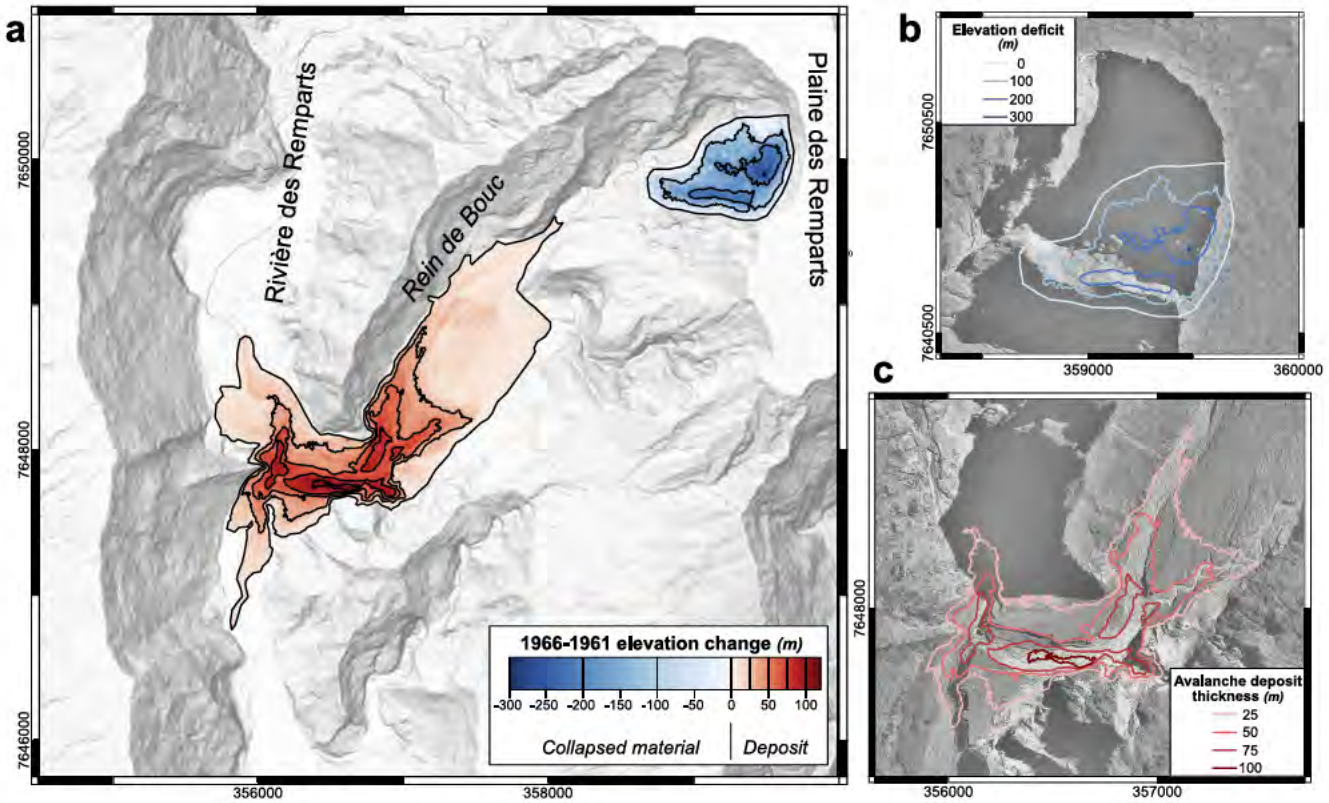

Figure 7. (a) Difference of DEM of the scar and of the deposit of the 1965 Mahavel landslide determined from the DEMs computed with the stereoscopic aerial images of IGN taken in 1961 and 1966. The background DEM provided by IGN represents the topography in 2003. Orthoimage of 1950 from IGN overlaid with the contour map of (b) the elevation deficit due to the scarp collapse during the 1965 Mahavel event and (c) the landslide deposit. Note that the largest deposit accumulations (thicker than 75 m) completely fill the channels of the initial topography. Coordinates in meter, WGS 84/UTM zone 40S.

flank opposite to the source area over elevations h_R ranging between 380 and 300 m at distances of 0.85 and 1.1 km from the source, respectively (step 1 in Figure 8). Following Chow's (1959) relationship,

$$v = \sqrt{2gh_R}, \tag{1}$$

where g is the gravitational acceleration, and the velocity v ranged between 77 and 86 m s^{-1} after these travel distances (Figure 10a). Then, in the Rein de Bouc section, the avalanche ran up the scarp of Rein de Bouc over an average elevation of around 130 m (step 2 in Figure 8). We determine flow velocities from two complementary approaches. According to McClung (2001) and Prochaska et al. (2008), the forced vortex equation from superelevation

$$v = \sqrt{\left(\frac{R_c g h_R}{kB}\right)}, \tag{2}$$

where R_c corresponds to the centerline radius of the bend (2,060 m), B the flow width (370 m) and k, a correction factor ranging between 1 and 5, suggests velocities between 38 and 85 m s^{-1}, respectively (Figure 10a). Moreover, to minimize the effect of the assumption on the correction factor k, Scheidl et al. (2015) proposed the empirical relationship from debris flow experiments in a curved-channel:

$$v = \left(\frac{R_c g \cos\cos\theta_c}{B} h_R\right)^{0.5} \left[\left(\frac{R_c}{h}\right)^{0.73} \left(\frac{h_R}{B}\right)^{0.73} 4.4^{-1.23}\right], \tag{3}$$

where θ_c and h accounts for the channel longitudinal slope and the average flow height, respectively. Considering an average slope θ_c of 7° and an average height h of 80 m, the superelevation on the scarp of Rein de Bouc would result from a flow velocity of 68 m s^{-1} (Figure 10a).

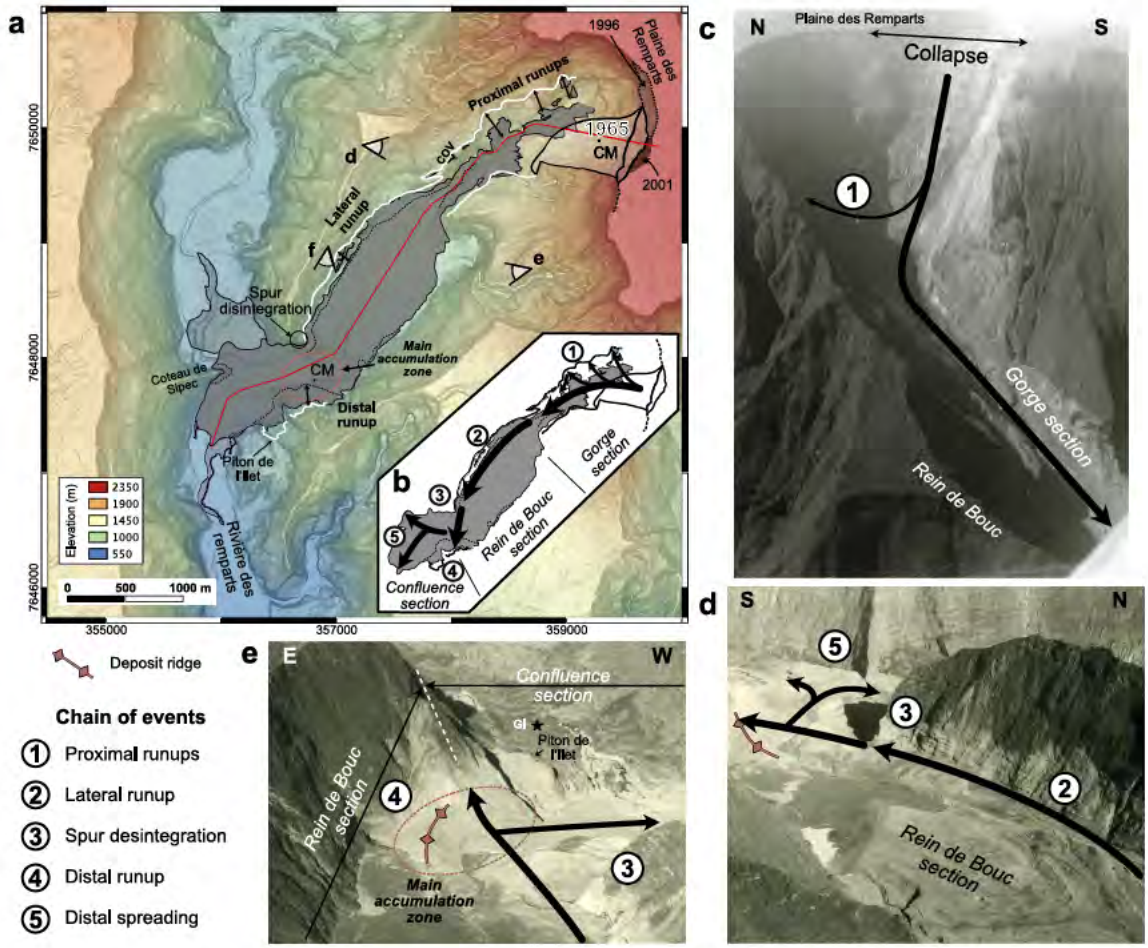

Figure 8. Chain of events during the 1965 Mahavel landslide. (a) Landslide deposit (dark gray area), trimline (white line) and runups on the scarps of the Bras de Mahavel tributary. The light gray zones account for the remobilized deposits observed in 1966. COV: Cap des Oiseaux Verts. Coordinates in meter, WGS 84/UTM zone 40S. (b) Sketch of the chain of events associated with the flow. The thick black arrows indicate the flow path suggested by the aerial photographs (c–e). Remobilized deposits appear in dark gray in the downstream part of the Rein de Bouc section (d, e). Note in (e) that the Grande Ilet hamlet was protected by the relief of Piton de l'Ilet. Photos: J. Legros.

At step 4, where a runup of 100 m is observed on the southern bank, a velocity of ~44 m s^{-1} can be determined from Equation 1. Interestingly, the lack of any runup on the scarp of Coteau de Sipec, that is, the western scarp of the Rivière des Remparts valley, suggests a slow velocity during step 5 and consequently a sharp velocity decrease between steps 4 and 5 until a stop after a horizontal travel of 5 km (Figure 10a).

Another way to assess the flow velocity of the Mahavel landslide is from the vertical drop h_{CM} of the center of mass that gives the maximum velocity of this center of mass (Ekström & Stark, 2013; Yamada et al., 2018):

$$v = 0.45\sqrt{2gh_{\mathrm{CM}}}\,. \tag{4}$$

The elevation of the centers of mass of the fallen pile of rocks and of the deposit can be estimated at around 1,850 m and 750–800 m from pre- and post-collapse topographies, respectively (Figure 10b). The vertical drop yields a maximum velocity of the center of mass of ~65 m s^{-1}.

4.4.2. Numerical Simulation

Since our numerical simulations are based on the SHALTOP model, which assumes the conservation of mass (i.e., incompressible fluid), and because the very steep topography of the collapsed cliff may induce uncertainties on the calculated volume of collapsed material, we choose to simulate the landslide by considering the volume of the landslide deposit derived from the photogrammetry following Sosio et al. (2008). Our simulations show a

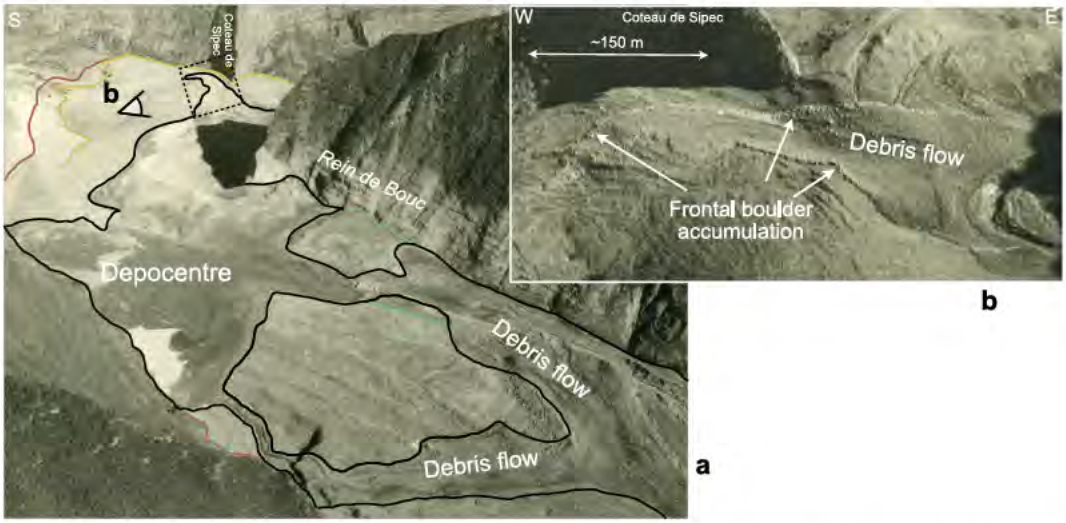

Figure 9. Remobilization of the landslide deposit. Heavy rainfalls produced debris flows that partially covered the primary landslide deposit and accumulated in a depocentre located in the downstream part of the Rein de Bouc section (a). Zoom on the debris flow unit characterized by a classical bouldery front (b). The color of the contours is similar to Figure 4 and these contours delimit de landslide units.

deposit close in extension to that observed in the field (Figure 11; Movie S1 in Supporting Information S2). This illustrates that the frictional model (i.e., Coulomb rheology with a depth-integrated friction coefficient δ of 9°), with conservation of mass, both well explains the deposition of the landslide to first order.

The simulation offers robust information on the dynamics of the landslide. It first suggests that the path of the center of mass is not rectilinear and follows the complex topography, in good agreement with the deductions from the photograph observations (Figure 11). Furthermore, the simulated velocity of the center of mass presents initial acceleration up to 48 m s^{-1} at t = 10 s, followed by a velocity oscillation until a maximum of 54 m s^{-1} reached in the narrowest part of the gorge section at t = 60 s (Figure 10b). It is worth noting that this initial complex velocity evolution of the center of mass occurred in the horseshoe-shaped upper part of the gorge section while part of the flow was running up and down the valley scarps. The simulated velocity of the center of mass then progressively decreased until half of the Rein de Bouc section, where it experienced two successive drops at t = 130 and 180 s after the landslide initiation (Figure 10b). The landslide-simulated velocity finally decreased from 4 m s^{-1} to its stop in the Rein de Bouc section in about 150 s. From its initiation to its halt, the flow lasted around 5 min and 45 s with a time average velocity of ~21 m s^{-1} (Figure 10b).

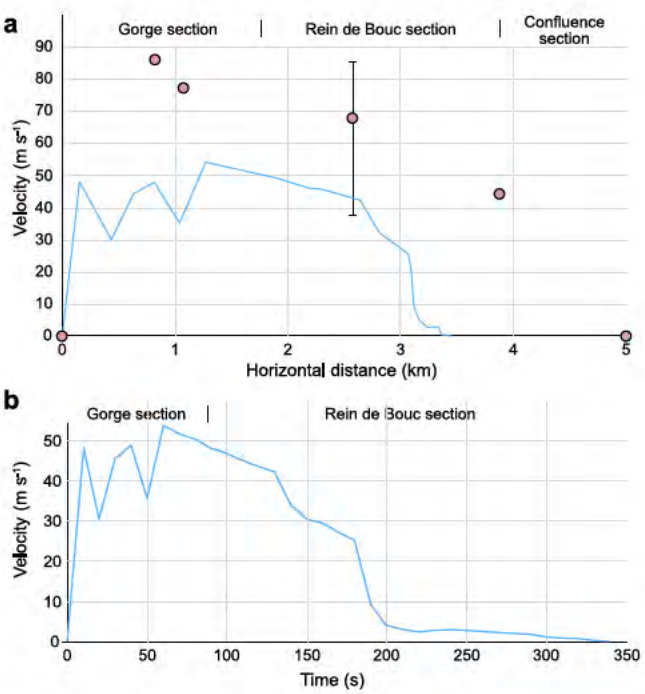

Figure 10. (a) Velocity of the landslide determined from the runup elevations along the flow path (pink circles) and of the center of mass from the simulation (blue curve). (b) Evolution of the simulated velocity at the center of mass over time.

The second result of our simulations concerns the trimline on the northern slope of Mahavel. Indeed, it confirms the deductions of the field regarding the passage of the landslide at the level of this boundary and this is therefore explained by the curvature forces applied by the topography on the flow. Moreover, the simulated maximum velocities are around 90–120 m s^{-1}, confirming again the previous deductions and emphasizing the high energy impact along this trimline.

Nevertheless, we note differences between the resulting deposits from the simulations and those obtained by photogrammetry. Upstream, the simulation predicts residual deposits in the gorge section that are absent in the post-event DEM. Yet, as mentioned in Section 4.1., these deposits are visible on the photos of J. Legros taken shortly after the landslide but were mostly remobilized before the IGN campaign of April 1966 used to build the DEM.

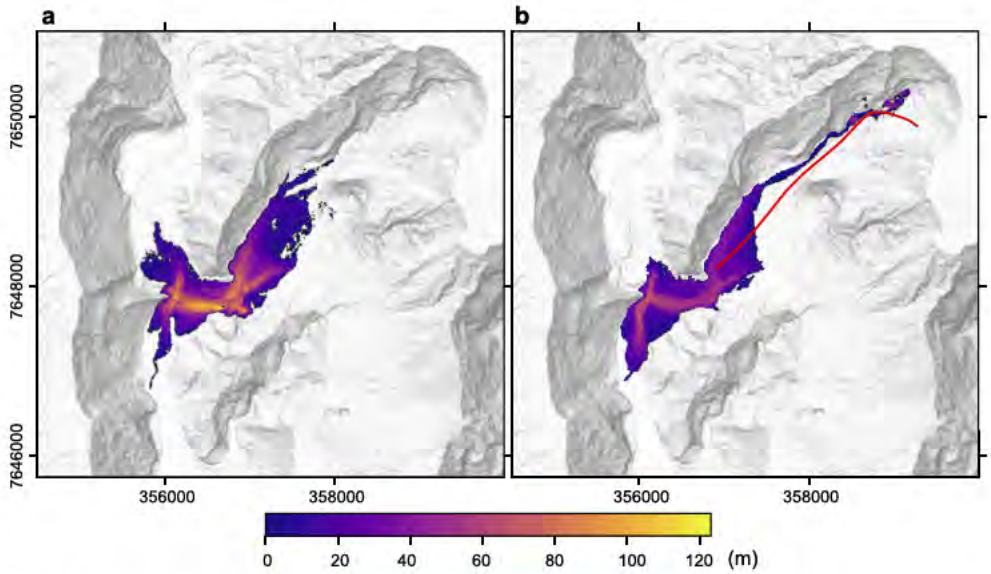

Figure 11. Deposits derived from DoD (a) and deposits simulated with SHALTOP model using Coulomb rheology ($\delta = 9°$) (b). Colormap scaled with the thickness in meters. The red curve accounts for the center of mass trajectory derived from the simulation.

Moreover, these deposits were located in a steep canyon and partly in the shadows. Hence, the DEM reconstruction using photogrammetry is less accurate/robust in this zone and may miss the deposit. Nonetheless, the simulation suggests that about 8% of the total volume stalled in the upstream part of the Bras de Mahavel tributary, which agrees well with the volume estimate made from the photographs of J. Legros in Section 4.1.

Finally, the morphology of the deposit front is not in perfect agreement with that obtained by field mapping and photogrammetry. This can be explained either by poor restitution of the initial mass, thus slightly affecting the simulated dynamics, or by the fact that the landslide occurred in different phases with post-event remobilization, which is discussed in the next section. Nevertheless, it should be noted that the morphology and extent of the deposit are mainly controlled by the bottom topography (e.g., Lucas et al., 2007, 2011). Thus, even using the collapsed volume of 60 Mm^3 (instead of the deposited volume of 46 Mm^3 as presented in this section and in Figure 11) we can produce a simulation in agreement with the observations by dissipation adjustment (Figure S4 in Supporting Information S1; see discussion in Lucas et al., 2011).

5. Discussion

5.1. Volume Balance

As mentioned above and shown in geomorphological reconstructions of volcanic provinces (e.g., Roberti et al., 2021), surface reconstruction by photogrammetry on very steep topography can lead to large uncertainties on the derived volumes. Our results suggest a large volume deficit of around 14 Mm^3 for the avalanche. Albeit this value falls in the range of volume uncertainty, it would imply a bulking factor ≤ 1 (0.77) between the source region and the deposit that differs from the bulking factors of 1.07–1.3 commonly determined for rock avalanches worldwide (e.g., Chen et al., 2006; Claude et al., 2014; Evans & Bent, 2004; Evans et al., 2001; Hungr & Evans, 2004; Stock & Uhrhammer, 2010).

In the case of Mahavel avalanche, three main hypotheses can be put forward to explain a volume deficit or, at min, a lack of volume increase of the deposit. It may stem from (a) a significant sediment accumulation in the gorge section that is not integrated in our estimate of the deposit volume (as shown by the simulation, part of the deposit could have rested in the narrow path between the headwall and the main gorge), (b) the transport of the deposit between the landslide event and the acquisition of the stereoscopic aerial photographs in 1966 (since part of the deposit may have been transported by the flowing river in one year time period), and/or (c) a porosity of the geological formations of the source area larger than in the deposit. Photographs from J. Legros reveal that

part of the deposit accumulated in the gorge section after the collapse of the headwall scarp. They correspond to a volume of 4–5 Mm^3 mostly concentrated at the base of the scar. Nonetheless, this volume is too small to explain the entire volume deficit between the pile of fallen rocks and the landslide deposit. Alternatively, the comparison of the deposit geometry on the photos of J. Legros (Figure 4) and the orthoimage of 1966 reconstructed from IGN images (Figure 2b), taken shortly after and one year after the landslide, respectively, reveal a partial remobilization of the deposit and lateral sediment transport of less than 1 km upstream and downstream the Rivière des Remparts (Figure 8a). However, since this deposit is integrated in our volume quantification, a lateral transport of a significant part of the avalanche deposit can therefore be ruled out (Figure 7). The third hypothesis invokes a porosity difference between the source and the deposit. As mentioned above, the collapsed material was made of 'a'ā lava flows and scoria deposits. The volcanic rock vesicularity significantly varies with the type of formations from 45% to 60% for scoria to around 25% for the lava flow massive core (Bato et al., 2016; Di Muro et al., 2014, 2021; Harris et al., 2017). Since the geological formations involved in the scarp collapse are dominantly scoria layers, an average vesicularity of around 35%–45% is a reasonable estimate for the total volume of rock. Rock avalanches experience intense particle fragmentation during their travel (e.g., Crosta et al., 2007; Perinotto et al., 2015). We therefore interpret the volume deficit between the deposit and the source as primarily resulting from the reduction of the initial volume by the destruction of the vesicularity due to fragmentation, while fragmentation usually yields a volume expansion (Hungr & Evans, 2004). Moreover, our data suggest that sediment entrainment by the rock avalanche during its travel on the valley floor, if any, was very limited. The sole obvious assimilation is the spur of Rein de Bouc that was destroyed during the avalanche (step 3 in Figure 8).

5.2. Conditioning Factors and Collapse Triggers

Rockslide and rock/debris avalanches result from modifications in the geophysical stresses and/or of the hydrometeorological conditions (e.g., Erismann & Abele, 2001; Keefer, 1984; Lu & Godt, 2013; Martha et al., 2015; Xing et al., 2017). All these changes may act at two different time scales. At a long time scale (i.e., few weeks to several thousand years), rock weathering, climatic changes or recurrent earthquakes, namely the conditioning factors, may induce a progressive fatigue and weakening of the rock mass subsequently prone to failure (Gischig et al., 2015, 2016; Jaboyedoff et al., 2004; Regmi et al., 2013; Sartori et al., 2003). At a short time scale (i.e., a few minutes to a few days), triggers such as large seismic events or intense rainfalls are able to produce the sudden destabilization of deep-seated rock mass (e.g., Crosta et al., 2004; Evans, Roberts, et al., 2009; Keefer et al., 1987).

Since the 1965 avalanche, two other collapse events characterized by successive rockfalls occurred in 1995 and 2001 in the headwall of the Mahavel canyon (Garcin et al., 2005; Rousseau, 1999). These events, much smaller in volume, led to deposit accumulation restricted to the gorge section. In each case (1965, 1995, and 2001), the scarp destabilization followed intense rainfalls by 1 day (Figure 3; Figure S5 in Supporting Information S1). Moreover, despite a relatively small distance between the Bras de Mahavel headwall and the volcanic center of Piton de la Fournaise (6 km), the lack of any eruption and seismicity (monitored in 1995 and 2001) during these events suggests that the collapse of the Bras de Mahavel scarp was not initiated by volcano-related geophysical stress changes. We therefore propose that intense rainfall events and the related water infiltration (Iverson, 2000) are the primary triggers of the Bras de Mahavel scarp collapses.

Although scarp destabilizations systematically follow intense precipitations in Bras de Mahavel, one must emphasize that many other rain events did not lead to such landslides. This raises the question of the conditioning factors that promoted the failure of the Bras de Mahavel headwall. Progressive rock weathering is known to reduce slope stability (e.g., Jaboyedoff et al., 2004; Regmi et al., 2013). The 1965 avalanche deposit lacks any trace of weathered basaltic rocks or secondary mineralization in the lava flow vesicles, as observed in the weathered rocks of the dormant Piton des Neiges volcano (Bret, Join, et al., 2003; Figure 1a for location). Alternatively, macro-earthquakes may have progressively yield a rock mass fatigue, that is, a reduction of the rock mass strength. Piton de la Fournaise is a basaltic shield volcano whose magma transfer-related seismicity is characterized by a magnitude $M < 3$ (Duputel et al., 2021). Yet, larger earthquakes can occur during volcano-tectonic events like the 2007 caldera collapse (earthquakes with $4.4 < M_w < 5.4$; Duputel & Rivera, 2019). Moreover, this volcano experienced larger collapse events since the emplacement of the lava flows forming the headwall of the Bras de Mahavel canyon (i.e., recurrent collapses of the 8-km-wide Enclos Fouqué caldera between 5465 and 2971 calendar years BP and a main lateral flank collapse 40–60 ka; Merle et al., 2010; Ort et al., 2016). It

is therefore likely that several large volcano-tectonic earthquakes weaken the overall strength of the geological formations of the Bras de Mahavel headwall since 60 ka and promoted the scarp failure.

In addition to this background setting, it is remarkable to note that the collapse events of 1965, 1995, and 2001 were all preceded by the same climatic succession: 2–3 abnormally dry years, followed by 1–2 abnormally wet years, and eventually the scarp collapse during the next rainy season (Figure 3; Figure S5 in Supporting Information S1). It has been recently proposed that dry spells are as important as extreme rainfalls in landslide occurrence due to shrinking-swelling effects of clayey minerals (Tichavský et al., 2019). Despite any evidence of clay-rich formations in the geological succession of the Mahavel headwall, we hypothesize that strong annual climatic variations yield conditions promoting rock mass failures during intense rainfall events. We also speculate that a process similar to the shrinking-swelling effect could act in vesiculated volcanic formations and weakens the rock mass strength.

5.3. Flow Type and Dynamics

Although the 1965 Mahavel landslide has not been witnessed, it was usually interpreted as a debris flow as it occurred after heavy rainfalls (BRGM, 1965; Merle et al., 2008). Yet, our data provide compelling evidence to re-interpret the flow type of the Mahavel landslide.

Debris/mud flows behave as a viscous material with velocities that rarely exceed 30 m s^{-1} (Coussot & Meunier, 1996; Hungr et al., 1984; Pierson, 1998; Takahashi, 1981). By contrast, both analytical velocity estimates from runups and simulated flow velocity with SHALTOP of the 1965 Mahavel landslide suggest much more rapid flow dynamics with maximum velocities ranging between 70 and 120 m s^{-1} during half of the final traveled distance. Such velocities were likely influenced by the flow lateral confinement before entering the Rein de Bouc section. They are in the highest velocity range of those of recent rock avalanches (e.g., Val Pola, Ygong, Thurweiser, Kolka Glacier, Mount Meager, Joffre Peak rock avalanches, Crosta et al., 2004; Delaney & Evans, 2015; Evans, Tutubalina, et al., 2009; Favreau et al., 2010; Friele et al., 2020; Guthrie et al., 2012).

Debris flows are saturated flows whose water may originate from different sources (e.g., glacier/snow incorporation, landslide-related dam destruction, river assimilation; e.g., Hungr et al., 2001). Their path is channelized favoring water incorporation and longitudinal sorting, with the largest blocks concentrated in the flow front (Pierson, 1986). Such characteristics are clearly visible on the debris flows that result from the remobilization of the deposit of the Mahavel landslide (Figure 9), but not in the primary landslide deposits. Moreover, the landslide deposit shows sedimentary features (fragmented and sheared blocks, topographic ridges perpendicular to the flow; Figure S3 in Supporting Information S1) absent in debris flows and typical of rock avalanches (Dufresne et al., 2016; Roberti et al., 2017).

We therefore interpret the 1965 Mahavel landslide as a main rock avalanche resulting from the collapse of the valley scarp, likely favored by the intense rainfalls that occurred a few days before the destabilization (see Section 5.2). Its volume and geological setting make it an exceptional example of large rock avalanches on basaltic volcanoes that is not related to a lateral flank collapse but associated with relief erosion.

The origin of the rock avalanche mobility remains unclear and lacks any consensual explanation (e.g., Legros, 2002). It could stem from the reduction of internal friction restricted to the basal part of the flow due to a weak sediment layer beneath the flow (Watson & Wright, 1967), air or water incorporation (Fahnestock, 1978; Voight & Sousa, 1994), or the development of a molten layer (De Blasio & Elverhøi, 2008). The mobility of rock avalanche could also originate from the fluidization of the entire flow by air or water incorporation (Crandell et al., 1984; Kent, 1966). Finally, it could result from dynamic disintegration of the flow clasts (Gao et al., 2021; Schneider & Fisher, 1998) combined with frictional fluidization within the matrix related to the interactions of the fine particles (Perinotto et al., 2015).

The air fluidization efficiency was questioned by Legros (2002) to explain the avalanche mobility, since a lithostatic air pressure should be maintained in the flow by an unlikely continuous air supply. The Mahavel avalanche involved volcanic formations with an estimated vesicularity of 35%–45% and the destruction of this porosity could explain the bulking factor ≤ 1. Consequently, the flow-related fragmentation, which increases with distance (e.g., Dufresne et al., 2016), continuously released the air filling the lava vesicles. Thus, air fluidization of the flow by the air released from the vesicles may have, to a certain extent, influenced the mobility of the 1965

Mahavel avalanche. Moreover, the Mahavel avalanche occurred after two successive events of intense precipitations that likely fed floods of the Bras de Mahavel River. The effective porosity of the volcanic materials (lava flows and scoria layers) forming the Bras de Mahavel headwall was also probably partly saturated with water infiltration. In such a context, initial partial water saturation and water assimilation during the flow may have enhanced the mobility of the Mahavel avalanche. However, the lack of distal evolution from avalanche to debris flow suggests that the water saturation was limited. Finally, the grain size distribution of the deposit, the fractal dimensions and the presence of elongated jigsaw-blocks (Figures 5 and 6) suggest an intense flow-related clast and particle disintegration that could lead to (a) a dispersive dilatancy and (b) the production of fines that reduce clast interactions and consequently fluidize the avalanche (Perinotto et al., 2015). We see two main reasons to explain the intense fragmentation of the avalanche and its potential role in the avalanche mobility: the high vertical drop during the scarp collapse and the bottleneck-like confinement between steps 1 and 2 in the chain of events.

We consider that the three above-mentioned processes (air and water fluidization and dynamic disintegration) were involved in the mobility of the 1965 Mahavel avalanche and speculate that the effect of the dynamic disintegration dominates.

Our analysis of the Mahavel avalanche illustrates the consequences of a large collapse of the high scarp bounding the Rivière des Remparts valley. Albeit very dynamic, the 1965 Mahavel avalanche was strongly constrained by the steep relief. The overall curved trajectory (Figure 8b) led to a frontal impact in the southern wall located at the transition between the Rein de Bouc and confluence sections (step 4 if Figure 8). The extreme dynamics of the Mahavel avalanche together with the lateral and frontal confinement could explain the lack of large blocks at the flow surface. Aerial photographs suggest that the avalanche massively deposited after the frontal impact at the limit between the Rein de Bouc and confluence sections (main accumulation zone in Figure 8). It subsequently fed the secondary unit that slowly flew onto the basal main flow unit in the confluence section (Figures 4b and 4c). Despite huge differences in the volume involved (46 Mm^3 vs. 26 km^3) and the runout distances (5 vs. 40 km), the Mahavel and Socompa avalanches are both characterized by high velocity primary flows and slowly moving secondary flows being controlled by local topographies (Kelfoun et al., 2008). This suggests that the occurrence of each flow type and the transition from primary to secondary flows are controlled by similar processes that are independent of the volumes involved.

5.4. Rock Avalanche and Erosion in Réunion Island

Réunion Island has among the highest long-term erosion rates on Earth (7–10 mm yr^{-1} during the last 70 Kyrs; Gayer et al., 2019). Bret, Fèvre, et al. (2003) and Salvany et al. (2012) proposed that most of the volcanic debris avalanche deposits cropping out in the Réunion deeply incised valleys were the result of valley scarp collapses. Our analysis of the Mahavel landslide confirms that the collapse of a large volume of volcanic rocks is able to produce rock avalanches that present deposits with identical sedimentological characteristics to the volcanic debris avalanches described in Réunion. We therefore interpret the intense erosion in Réunion Island and the development of head amphitheater valleys as the result of recurrent deep-seated scarp collapses similar to the 1965 Mahavel one.

Furthermore, Gayer et al. (2019) revealed that erosion rates are one order of magnitude larger in the dry leeward side of the island compare to its wet winward side. This difference has been shown to be controlled by the variability in precipitation rates, that is, the larger the rainfall variability, the stronger the erosion rates (Gayer et al., 2019). Our results on the controlling factors of the Bras de Mahavel headwall collapses suggest that important annual precipitation variations favor scarp collapses (see Section 5.2). We consequently propose that the spatial precipitation variability observed at the island scale modulates the occurrence of scarp collapses (more frequent in the leeward side than in the winward part) and subsequently the long-term erosion rates. We finally anticipate that augmentation of the precipitation variability due to global climate changes (Pendergrass et al., 2017) could increase the occurrence the deep-seated landslides and rock avalanches in mountainous areas.

6. Conclusion

The main results of our analysis of the 1965 Mahavel landslide can be summarized as follows:

1. Historical images of J. Legros allows us to identify two types of flow units related to the 1965 Mahavel avalanche. They suggest the occurrence of a main avalanche unit that evolves in a spreading secondary flow in the confluence section.

2. The deposit of the main avalanche presents two facies (jigsaw-fracturated facies and matrix-rich fragmented facies) that are characterized by angular clasts, with abundant elongated, fragmented jigsaw blocks in the former and a predominance of a gravely-to-silty matrix in the latter. The fractal dimension of these facies range between 2.472 and 2.865, characteristic values for avalanche deposits.
3. Using (a) the stereoscopic images of IGN taken before and after the landslide, and (b) the photogrammetric procedure developed by Lucas and Gayer (2022), we quantified both the volumes of collapse material (59.7 ± 3.2 Mm^3) and the rock avalanche deposit (46 ± 13 Mm^3). We propose that the volume difference between the source and the deposit mainly results from the disintegration of the vesicularity of the volcanic rocks.
4. We characterized the dynamics of the avalanche with two complementary approaches. (a) Observations of the frontal and lateral runups indicate velocity between 77 and 86 m s^{-1} in the gorge section, decreasing to 44 m s^{-1} at the transition between the Rein de Bouc and confluence sections. At this point, a secondary flow slowly spread in the confluence section. (b) The simulations with SHALTOP confirm this dynamic and indicate that the avalanche traveled the total runout in about 5 min and 45 s. We propose that the avalanche mobility results from the combined effect of air and water fluidization and dynamic disintegration. Both fluids are thought to mainly originate from the destruction of the lava vesicules.
5. The 1965 Mahavel avalanche and two less important scarps collapse in 1995 and 2001 systematically occurred one day after heavy rainfalls. We consequently suggest that intense rainfalls and the related infiltrations are the main triggers of landslides in Réunion. Moreover, we propose that the climatic variability observed before each collapse event (succession of dry and wet years) brings conditions prone to rock mass failure. Such relationship could explain the long-term erosion rates difference between the dry leeward and wet windward sides of Réunion that are characterized by high and low precipitation variability, respectively. It also indicates that the occurrence of rock avalanche could increase in a warmer climate due to the augmentation of precipitation variability.

Data Availability Statement

Archive aerial photographs of the Institut Géographique National (IGN) are available for free at https://remonterletemps.ign.fr/. Historical picture of J. Legros are private items. DEMs have been built from the IGN images with the approach described in Lucas and Gayer (2022). Meteorological data of Météo France are available at https://publitheque.meteo.fr/.

Acknowledgments
This work has been supported by the Univerité de La Rénuion and the Programme National de Télédétecion Spatiale (PNTS, Grant PNTS-2022) and the LabEx UnivEarthS (ANR-10-LABX-0023 and ANR-18-IDEX-0001). We thank Météo France for their data and Matt Brain (Associate Editor), Gioachino Roberti (reviewer) and an anonymous reviewer for the constructive comments that allow to significantly improve this manuscript.

References

Ancey, C., & Meunier, M. (2004). Estimating bulk rheological properties of flowing snow avalanches from field data. *Journal of Geophysical Research*, *109*(F1), F01004. https://doi.org/10.1029/2003JF000036

Bachèlery, P., & Mairine, P. (1990). Evolution volcano-structurale du Piton de la Fournaise depuis 0.53 Ma. In *Le Volcanisme de La Réunion–Monographie* (pp. 213–242). Centre de Recherche en Volcanologie, Clermont-Ferrand.

Barcelo, A., & Coudray, J. (1996). New annual isohyet and rainfall maximum map for the Piton de la Fournaise massif (Reunion Island). *Journal of Water Science*, *9*(4), 457–484. https://doi.org/10.7202/705262ar

Bato, M. G., Froger, J. L., Harris, A. J. L., & Villeneuve, N. (2016). Monitoring an effusive eruption at Piton de la Fournaise using radar and thermal infrared remote sensing data: Insights into the October 2010 eruption and its lava flows. *Geological Society, London, Special Publications*, *426*(1), 533–552. https://doi.org/10.1144/SP426.30

Bouchut, F., Mangeney-Castelnau, A., Perthame, B., & Vilotte, J.-P. (2003). A new model of Saint Venant and Savage–Hutter type for gravity driven shallow water flows. *Comptes Rendus Mathématique de l'Académie des Sciences de Paris*, *336*(6), 531–536. https://doi.org/10.1016/S1631-073X(03)00117-1

Bouchut, F., & Westdickenberg, M. (2004). Gravity driven shallow water models for arbitrary topography. *Communications in Mathematical Sciences*, *2*(3), 359–389. https://doi.org/10.4310/cms.2004.v2.n3.a2

Bret, L., Fèvre, Y., Join, J.-L., Robineau, B., & Bachèlery, P. (2003). Deposits related to degradation processes on Piton des Neiges volcano (Reunion Island): Overview and geological hazard. *Journal of Volcanology and Geothermal Research*, *123*(1–2), 25–41. https://doi.org/10.1016/S0377-0273(03)00026-X

Bret, L., Join, J.-L., Legal, X., Coudray, J., & Fritz, B. (2003). Argiles et zéolites dans l'altération d'un volcan bouclier en milieu tropical (Le Piton des Neiges, La Réunion). *Comptes Rendus Geoscience*, *335*(14), 1031–1038. https://doi.org/10.1016/j.crte.2003.09.007

BRGM. (1965). L'éboulement du Rempart au lieu-dit "Le Bras de Mahavel". TAN 65-A/24, Technical report.

Chaput, M., Famin, V., & Michon, L. (2017). Sheet intrusions and deformation of Piton des Neiges, and their implication for the volcano-tectonics of La Réunion. *Tectonophysics*, *717*, 531–546. https://doi.org/10.1016/j.tecto.2017.08.039

Chen, R.-F., Chang, K.-J., Angelier, J., Chan, Y.-C., Deffontaines, B., Lee, C.-T., & Lin, M.-L. (2006). Topographical changes revealed by high-resolution airborne LiDAR data: The 1999 Tsaoling landslide induced by the Chi–Chi earthquake. *Engineering Geology*, *88*(3–4), 160–172. https://doi.org/10.1016/j.enggeo.2006.09.008

Chow, V. T. (1959). *Open-channel hydraulics*. McGraw-Hill.

Claude, A., Ivy-Ochs, S., Kober, F., Antognini, M., Salcher, B., & Kubik, P. W. (2014). The chironico landslide (Valle Leventina, southern Swiss Alps): Age and evolution. *Swiss Journal of Geosciences*, *107*(2–3), 273–291. https://doi.org/10.1007/s00015-014-0170-z

Costa, J. E. (1991). Nature, mechanics, and mitigation of the Val Pola landslide, Valtellina, Italy, 1987–1988. *Zeitschrift für Geomorphologie*, *35*(1), 15–38. https://doi.org/10.1127/zfg/35/1991/15

Coussot, P., & Meunier, M. (1996). Recognition, classification and mechanical description of debris flows. *Earth-Science Reviews*, *40*(3–4), 209–227. https://doi.org/10.1016/0012-8252(95)00065-8

Crandell, D. R., Miller, C. D., Glicken, H., Christiansen, R. L., & Newhall, C. G. (1984). Catastrophic debris avalanche from ancestral Mount Shasta volcano, California. *Geology*, *12*(3), 143–146. https://doi.org/10.1130/0091-7613(1984)12<143:cdafam>2.0.co;2

Crosta, G. B., Chen, H., & Lee, C. F. (2004). Replay of the 1987 Val Pola landslide, Italian Alps. *Geomorphology*, *60*(1–2), 127–146. https://doi.org/10.1016/j.geomorph.2003.07.015

Crosta, G. B., Frattini, P., & Fusi, N. (2007). Fragmentation in the Val Pola rock avalanche, Italian Alps. *Journal of Geophysical Research*, *112*(F1), F01006. https://doi.org/10.1029/2005JF000455

De Blasio, V. F., & Elverhøi, A. (2008). A model for frictional melt production beneath large rock avalanches. *Journal of Geophysical Research*, *113*(F2), F02014. https://doi.org/10.1029/2007JF000867

de Cordemoy, E. J. (1876). *Rapport de la Commission chargée d'étudier la catastrophe du Grand-Sable, à Salazie*. Typ. de Gabriel Lahuppe.

Delaney, K. B., & Evans, S. G. (2015). The 2000 Yigong landslide (Tibetan Plateau), rockslide-dammed lake and outburst flood: Review, remote sensing analysis, and process modelling. *Geomorphology*, *246*, 377–393. https://doi.org/10.1016/j.geomorph.2015.06.020

Di Muro, A., Metrich, N., Vergani, D., Rosi, M., Armienti, P., Fougeroux, T., et al. (2014). The shallow plumbing system of Piton de la Fournaise volcano (La Reunion Island, Indian Ocean) revealed by the major 2007 caldera-forming eruption. *Journal of Petrology*, *55*(7), 1287–1315. https://doi.org/10.1093/petrology/egu025

Di Muro, A., Schwarzlmueller, F., Kueppers, U., Heap, M., & Dingwell, D. (2021). Petrophysical characterisation of volcanic ejecta to constrain subsurface lithological heterogeneities: Implications for edifice stability at basaltic volcanoes. *Volcanica*, *4*(1), 41–66. https://doi.org/10.30909/vol.04.01.4166

Duffield, W. A., Stieltjes, L., & Varet, J. (1982). Huge landslide blocks in the growth of Piton de la Fournaise, La Reunion, and Kilauea volcano, Hawaii. *Journal of Volcanology and Geothermal Research*, *12*(1–2), 147–160. https://doi.org/10.1016/0377-0273(82)90009-9

Dufresne, A., Bösmeier, A., & Prager, C. (2016). Sedimentology of rock avalanche deposits—Case study and review. *Earth-Science Reviews*, *163*, 234–259. https://doi.org/10.1016/j.earscirev.2016.10.002

Dufresne, A., & Dunning, S. A. (2017). Process dependence of grain size distributions in rock avalanche deposits. *Landslides*, *14*(5), 1555–1563. https://doi.org/10.1007/s10346-017-0806-y

Duputel, Z., Ferrazzini, V., Lengliné, O., Michon, L., Fontaine, F. R., & Massin, F. (2021). Seismicity of La Réunion Island. *Comptes Rendus Geoscience*, *353*(S1), 237–255. https://doi.org/10.5802/crgeos.77

Duputel, Z., & Rivera, L. (2019). The 2007 caldera collapse of Piton de la Fournaise volcano: Source process from very-long-period seismic signals. *Earth and Planetary Science Letters*, *527*, 115786. https://doi.org/10.1016/j.epsl.2019.115786

Ekström, G., & Stark, C. P. (2013). Simple scaling of catastrophic landslide dynamics. *Science*, *339*(6126), 1416–1419. https://doi.org/10.1126/science.1232887

Erismann, T. H., & Abele, G. (2001). *Dynamics of rockslides and rockfalls* (p. 316). Springer-Verlag.

Evans, S. G. (2006). Single-event landslides resulting from massive rock slope failure: Characterising their frequency and impact on society. In *Landslides from massive rock failure, NATO science series* (pp. 53–73). Springer.

Evans, S. G., & Bent, A. L. (2004). The Las Colinas landslide, Santa Tecla: A highly destructive flowslide triggered by the January 13, 2001, El Salvador earthquake. In W. I. Rose, J. J. Bommer, D. L. López, M. J. Carr, & J. J. Major (Eds.), *Natural hazards in El Salvador, special publications* (pp. 25–37). Geological Society of America. https://doi.org/10.1130/0-8137-2375-2.25

Evans, S. G., Hungr, O., & Clague, J. J. (2001). Dynamics of the 1984 rock avalanche and associated distal debris flow on Mount Cayley, British Columbia, Canada; implications for landslide hazard assessment on dissected volcanoes. *Engineering Geology*, *61*(1), 29–51. https://doi.org/10.1016/s0013-7952(00)00118-6

Evans, S. G., Roberts, N. J., Ischuk, A., Delaney, K. B., Morozova, G. S., & Tutubalina, O. (2009). Landslides triggered by the 1949 Khait earthquake, Tajikistan, and associated loss of life. *Engineering Geology*, *109*(3–4), 195–212. https://doi.org/10.1016/j.enggeo.2009.08.007

Evans, S. G., Tutubalina, O. V., Drobyshev, V. N., Chernomorets, S. S., McDougall, S., Petrakov, D. A., & Hungr, O. (2009). Catastrophic detachment and high-velocity long-runout flow of Kolka Glacier, Caucasus Mountains, Russia in 2002. *Geomorphology*, *105*(3–4), 314–321. https://doi.org/10.1016/j.geomorph.2008.10.008

Fahnestock, R. K. (1978). Little Tahoma Peak rockfalls and avalanches, Mount Rainier, Washington, USA. In B. Voight (Ed.), *Rockslides and avalanches: Natural phenomena* (Vol. 1, pp. 181–196). Elsevier.

Favreau, P., Mangeney, A., Lucas, A., Crosta, G., & Bouchut, F. (2010). Numerical modeling of landquakes. *Geophysical Research Letters*, *37*(15), L15305. https://doi.org/10.1029/2010GL043512

France, M. (2023). Données publiques [WWW document]. Retrieved from https://donneespubliques.meteofrance.fr

Friele, P., Millard, T. H., Mitchell, A., Allstadt, K. E., Menounos, B., Geertsema, M., & Clague, J. J. (2020). Observations on the May 2019 Joffre Peak landslides, British Columbia. *Landslides*, *17*(4), 913–930. https://doi.org/10.1007/s10346-019-01332-2

Gao, G., Meguid, M. A., Chouinard, L. E., & Zhan, W. (2021). Dynamic disintegration processes accompanying transport of an earthquake-induced landslide. *Landslides*, *18*(3), 909–933. https://doi.org/10.1007/s10346-020-01508-1

Garcin, M., Poisson, B., & Pouget, R. (2005). High rates of geomorphological processes in a tropical area: The Remparts River case study (Réunion Island, Indian Ocean). *Geomorphology*, *67*(3–4), 335–350. https://doi.org/10.1016/j.geomorph.2004.11.002

Gayer, E., Michon, L., Louvat, P., & Gaillardet, J. (2019). Storm-induced precipitation variability control of long-term erosion. *Earth and Planetary Science Letters*, *517*, 61–70. https://doi.org/10.1016/j.epsl.2019.04.003

Gayer, E., Michon, L., & Villeneuve, N. (2021). Volcanic island multi-stage construction inferred from a simple geometrical approach: Example of Réunion Island. *Geomorphology*, *392*, 107900. https://doi.org/10.1016/j.geomorph.2021.107900

Gillot, P. Y., Lefèvre, J. C., & Nativel, P. E. (1994). Model for the structural evolution of the volcanoes of Réunion Island. *Earth and Planetary Science Letters*, *122*(3–4), 291–302. https://doi.org/10.1016/0012-821x(94)90003-5

Gischig, V., Preisig, G., & Eberhardt, E. (2016). Numerical investigation of seismically induced rock mass fatigue as a mechanism contributing to the progressive failure of deep-seated landslides. *Rock Mechanics and Rock Engineering*, *49*(6), 2457–2478. https://doi.org/10.1007/s00603-015-0821-z

Gischig, V. S., Eberhardt, E., Moore, J. R., & Hungr, O. (2015). On the seismic response of deep-seated rock slope instabilities—Insights from numerical modeling. *Engineering Geology*, *193*, 1–18. https://doi.org/10.1016/j.enggeo.2015.04.003

Guthrie, R. H., Friele, P., Allstadt, K., Roberts, N., Evans, S. G., Delaney, K. B., et al. (2012). The 6 August 2010 Mount Meager rock slide-debris flow, Coast Mountains, British Columbia: Characteristics, dynamics, and implications for hazard and risk assessment. *Natural Hazards and Earth System Sciences*, *12*(5), 1277–1294. https://doi.org/10.5194/nhess-12-1277-2012

Harris, A. J. L., Villeneuve, N., Di Muro, A., Ferrazzini, V., Peltier, A., Coppola, D., et al. (2017). Effusive crises at Piton de la Fournaise 2014–2015: A review of a multi-national response model. *Journal of Applied Volcanology*, *6*(1), 11. https://doi.org/10.1186/s13617-017-0062-9

Hibert, C., Mangeney, A., Grandjean, G., & Shapiro, N. M. (2011). Slope instabilities in Dolomieu crater, Réunion Island: From seismic signals to rockfall characteristics. *Journal of Geophysical Research*, *116*(F4), F04032. https://doi.org/10.1029/2011JF002038

Hildenbrand, A., Gillot, P.-Y., & Marlin, C. (2008). Geomorphological study of long-term erosion on a tropical volcanic ocean island: Tahiti-Nui (French Polynesia). *Geomorphology*, *93*(3–4), 460–481. https://doi.org/10.1016/j.geomorph.2007.03.012

Hooke, R. L., & Iverson, N. R. (1995). Grain-size distribution in deforming subglacial tills: Role of grain fracture. *Geology*, *23*(1), 57–60. https://doi.org/10.1130/0091-7613(1995)023<0057:gsdids>2.3.co;2

Hungr, O., & Evans, S. G. (2004). Entrainment of debris in rock avalanches: An analysis of a long run-out mechanism. *Geological Society of America Bulletin*, *116*(9), 1240–1313. https://doi.org/10.1130/B25362.1

Hungr, O., Evans, S. G., Bovis, M. J., & Hutchinson, J. N. (2001). *A review of the classification of landslides of the flow type* (pp. 221–238). Environmental and Engineering Geoscience VII.

Hungr, O., Leroueil, S., & Picarelli, L. (2014). The Varnes classification of landslide types, an update. *Landslides*, *11*(2), 167–194. https://doi.org/10.1007/s10346-013-0436-y

Hungr, O., Morgan, G. C., & Kellerhals, R. (1984). Quantitative analysis of debris torrent hazards for design of remedial measures. *Canadian Geotechnical Journal*, *21*(4), 663–677. https://doi.org/10.1139/t84-073

Iverson, R. M. (2000). Landslide triggering by rain infiltration. *Water Resources Research*, *36*(7), 1897–1910. https://doi.org/10.1029/2000WR900090

Jaboyedoff, M., Baillifard, F., Bardou, E., & Girod, F. (2004). The effect of weathering on Alpine rock instability. *The Quarterly Journal of Engineering Geology and Hydrogeology*, *37*(2), 95–103. https://doi.org/10.1144/1470-9236/03-046

Keefer, D. K. (1984). Landslides caused by earthquakes. *Geological Society of America Bulletin*, *95*(4), 406–421. https://doi.org/10.1130/0016-7606(1984)95<406:lcbe>2.0.co;2

Keefer, D. K., Wilson, R. C., Mark, R. K., Brabb, E. E., Brown, W. M., Ellen, S. D., et al. (1987). Real-time landslide warning during heavy rainfall. *Science*, *238*(4829), 921–925. https://doi.org/10.1126/science.238.4829.921

Kelfoun, K., Druitt, T., van Wyk de Vries, B., & Guilbaud, M.-N. (2008). Topographic reflection of the Socompa debris avalanche, Chile. *Bulletin of Volcanology*, *70*(10), 1169–1187. https://doi.org/10.1007/s00445-008-0201-6

Kent, P. (1966). The transport mechanism in catastrophic rock falls. *The Journal of Geology*, *74*(1), 79–83. https://doi.org/10.1086/627142

Legros, F. (2002). The mobility of long-runout landslides. *Engineering Geology*, *63*(3–4), 301–331. https://doi.org/10.1016/s0013-7952(01)00090-4

Lu, N., & Godt, J. W. (2013). *Hillslope hydrology and stability* (p. 437). Cambridge University Press.

Lucas, A., & Gayer, E. (2022). Decennial geomorphic transport from archived time Series digital elevation models: A cookbook for tropical and Alpine environments. *IEEE Geoscience and Remote Sensing Magazine*, *10*(2), 120–134. https://doi.org/10.1109/mgrs.2021.3121370

Lucas, A., & Mangeney, A. (2007). Mobility and topographic effects for large Valles Marineris landslides on Mars. *Geophysical Research Letters*, *34*(10), L10201. https://doi.org/10.1029/2007GL029835

Lucas, A., Mangeney, A., & Ampuero, J. (2014). Frictional velocity-weakening in landslides on Earth and on other planetary bodies. *Nature Communications*, *5*(1), 3417. https://doi.org/10.1038/ncomms4417

Lucas, A., Mangeney, A., Bouchut, F., Bristeau, M. O., & Mège, D. (2007). Benchmarking exercises for granular flows. In K. Ho & V. Li (Eds.), *Proceedings of the 2007 international forum on landslide disaster management, Hong Kong, 10–12 December 2007*. Hong Kong institution of engineers.

Lucas, A., Mangeney, A., Mège, D., & Bouchut, F. (2011). Influence of the scar geometry on landslide dynamics and deposits: Application to Martian landslides. *Journal of Geophysical Research*, *116*(E10), E10001. https://doi.org/10.1029/2011JE003803

Mairine, P., & Bachèlery, P. (1997). Un grand épisode érosionnel dans l'histoire ancienne du Piton de la Fournaise. *Comptes Rendus de l'Académie des Sciences Paris*, *325*(4), 243–249. https://doi.org/10.1016/s1251-8050(97)88296-1

Mangeney, A., Bouchut, F., Thomas, N., Vilotte, J. P., & Bristeau, M. O. (2007). Numerical modeling of self-channeling granular flows and of their levee-channel deposits. *Journal of Geophysical Research*, *112*(F2), F02017. https://doi.org/10.1029/2006JF000469

Mangeney-Castelnau, A., Bouchut, F., Vilotte, J. P., Lajeunesse, E., Aubertin, A., & Pirulli, M. (2005). On the use of Saint Venant equations to simulate the spreading of a granular mass. *Journal of Geophysical Research*, *110*(B9), B09103. https://doi.org/10.1029/2004JB003161

Martha, T. R., Roy, P., Govindharaj, K. B., Kumar, K. V., Diwakar, P. G., & Dadhwal, V. K. (2015). Landslides triggered by the June 2013 extreme rainfall event in parts of Uttarakhand state, India. *Landslides*, *12*(1), 135–146. https://doi.org/10.1007/s10346-014-0540-7

McClung, D. M. (2001). Superelevation of flowing avalanches around curved channel bends. *Journal of Geophysical Research*, *106*(B8), 16489–16498. https://doi.org/10.1029/2001jb000266

McDougall, I. (1971). The geochronology and evolution of the young volcanic island of Réunion, Indian Ocean. *Geochimica et Cosmochimica Acta*, *35*(3), 261–288. https://doi.org/10.1016/0016-7037(71)90037-8

Merle, O., Mairine, P., Michon, L., Bachèlery, P., & Smietana, M. (2010). Calderas, landslides and paleo-canyons on Piton de la Fournaise volcano (La Reunion Island, Indian Ocean). *Journal of Volcanology and Geothermal Research*, *189*(1–2), 131–142. https://doi.org/10.1016/j.jvolgeores.2009.11.001

Merle, O., Michon, L., & Bachèlery, P. (2008). Caldera rim collapse: A hidden volcanic hazard. *Journal of Volcanology and Geothermal Research*, *177*(2), 525–530. https://doi.org/10.1016/j.jvolgeores.2008.06.011

Moretti, L., Allstadt, K., Mangeney, A., Capdeville, Y., Stutzmann, E., & Bouchut, F. (2015). Numerical modeling of the Mount Meager landslide constrained by its force history derived from seismic data. *Journal of Geophysical Research-Solid Earth*, *120*(4), 2579–2599. https://doi.org/10.1002/2014JB011426

Ort, M. H., Di Muro, A., Michon, L., & Bachèlery, P. (2016). Explosive eruptions from the interaction of magmatic and hydrothermal systems during flank extension: The Bellecombe Tephra of Piton de La Fournaise (La Réunion Island). *Bulletin of Volcanology*, *78*(1), 5. https://doi.org/10.1007/s00445-015-0998-8

Pendergrass, A. G., Knutti, R., Lehner, F., Deser, C., & Sanderson, B. M. (2017). Precipitation variability increases in a warmer climate. *Scientific Reports*, *7*(1), 17966. https://doi.org/10.1038/s41598-017-17966-y

Perinotto, H., Schneider, J. L., Bachèlery, P., Le Bourdonnec, F.-X., Famin, V., & Michon, L. (2015). The extreme mobility of debris avalanches: A new model of transport mechanism. *Journal of Geophysical Research-Solid Earth*, *120*(12), 8110–8119. https://doi.org/10.1002/2015JB011994

PGRI. (2009). Mission d'étude générale (P.G.R.I.) de la Rivière des Remparts—Commune de Saint-Joseph. Phase 2: Caractérisation du fonctionnement hydrogéomorphologique de la rivière. Technical report no 4700546 R2. (p. 265).

Pierson, T. C. (1986). Flow behavior of channelized debris flows, Mount St. helens, Washington. Chapter 13. In A. D. Abrahams (Ed.), *Hillslope processes: Binghamton geomorphology symposium 16* (pp. 269–296). Allen & Unwin.

Pierson, T. C. (1998). An empirical method for estimating travel times for wet volcanic mass flows. *Bulletin of Volcanology*, *60*(2), 98–109. https://doi.org/10.1007/s004450050219

Prochaska, A. B., Santi, P. M., Higgins, J. D., & Cannon, S. H. (2008). A study of methods to estimate debris flow velocity. *Landslides*, *5*(4), 431–444. https://doi.org/10.1007/s10346-008-0137-0

Réchou, A., Flores, O., Jumaux, G., Duflot, V., Bousquet, O., Pouppeville, C., & Bonnardot, F. (2019). Spatio-temporal variability of rainfall in a high tropical island: Patterns and large-scale drivers in Réunion Island. *Quaterly Journal of the Royal Meteorological Society*, *145*(720), 893–909. https://doi.org/10.1002/qj.3485

Regmi, A. D., Yoshida, K., Dhital, M. R., & Devkota, K. (2013). Effect of rock weathering, clay mineralogy, and geological structures in the formation of large landslide, a case study from Dumre Besei landslide, Lesser Himalaya Nepal. *Landslides*, *10*, 1–13. https://doi.org/10.1007/s10346-011-0311-7

Richards, M. A., Duncan, R. A., & Courtillot, V. E. (1989). Flood basalts and hot-spot tracks: Plume heads and tails. *Science*, *246*(4926), 103–107. https://doi.org/10.1126/science.246.4926.103

Roberti, G., Friele, P., van Wyk de Vries, B., Ward, B., Clague, J. J., Perotti, L., & Giardino, M. (2017). Rheological evolution of the Mount Meager 2010 debris avalanche, southwestern British Columbia. *Geosphere*, *13*(2), 369–390. https://doi.org/10.1130/GES01389.1

Roberti, G., Ward, B. C., van Wyk deVries, B., Perotti, L., Giardino, M., Friele, P. A., et al. (2021). Structure from motion used to revive archived aerial photographs for geomorphological analysis: An example from Mount Meager volcano, British Columbia, Canada. *Canadian Journal of Earth Sciences*, *58*(12), 1253–1267. https://doi.org/10.1139/cjes-2020-0140

Rousseau, N. (1999). Les signaux sismiques associes aux eboulements sur l'ile de la reunion (ocean indien)—Etude de 2 sites: la cascade de maha vel et la cavite de la soufriere. Unpublished PhD thesis. (Vol. *7*, P. 134). Université Paris.

Salvany, T., Lahitte, P., Nativel, P., & Gillot, P.-Y. (2012). Geomorphic evolution of the Piton des Neiges volcano (Réunion Island, Indian Ocean): Competition between volcanic construction and erosion since 1.4 Ma. *Geomorphology*, *136*(1), 132–147. https://doi.org/10.1016/j.geomorph.2011.06.009

Sartori, M., Baillifard, F., Jaboyedoff, M., & Rouiller, J. D. (2003). Kinematics of the 1991 Randa rockslides (Valais, Switzerland). *Natural Hazards and Earth System Sciences*, *3*(5), 423–433. https://doi.org/10.5194/nhess-3-423-2003

Scheidl, C., McArdell, B. W., & Rickenmann, D. (2015). Debris-flow velocities and superelevation in a curved laboratory channel. *Canadian Geotechnical Journal*, *52*(3), 305–317. https://doi.org/10.1139/cgj-2014-0081

Schneider, J. L., & Fisher, R. V. (1998). Transport and emplacement mechanisms of large volcanic debris avalanches: Evidence from the northwest sector of Cantal volcano (France). *Journal of Volcanology and Geothermal Research*, *83*(1–2), 141–165. https://doi.org/10.1016/s0377-0273(98)00016-x

Sherrod, D. R., Sinton, J. M., Watkins, S. E., & Brunt, K. M. (2021). *Geologic map of the state of Hawaii (report No. 3143)*. Scientific Investigations Map. https://doi.org/10.3133/sim3143

Sosio, R., Crosta, B. G., & Hungr, O. (2008). Complete dynamic modeling calibration for the Thurwieser rock avalanche (Italian Central Alps). *Engineering Geology*, *100*(1–2), 11–26. https://doi.org/10.1016/j.enggeo.2008.02.012

Stock, G. M., & Uhrhammer, R. A. (2010). Catastrophic rock avalanche 3600 years BP from El Capitan, Yosemite Valley, California. *Earth Surface Processes and Landforms*, *35*(8), 941–951. https://doi.org/10.1002/esp.1982

Takahashi, T. (1981). Debris flow. *Annual Review of Fluid Mechanics*, *13*(1), 57–77. https://doi.org/10.1146/annurev.fl.13.010181.000421

Tichavský, R., Ballesteros-Cánovas, J. A., Šilhán, K., Tolasz, R., & Stoffel, M. (2019). Dry spells and extreme precipitation are the main trigger of landslides in central Europe. *Scientific Reports*, *9*(1), 14560. https://doi.org/10.1038/s41598-019-51148-2

Voight, B., & Sousa, J. (1994). Lessons from Ontake-san: A comparative analysis of debris avalanche dynamics. *Engineering Geology*, *38*(3–4), 261–297. https://doi.org/10.1016/0013-7952(94)90042-6

Watson, R. A., & Wright, H. E. (1967). The Saidmarreh landslide, Iran. *Geological Society of America Special Paper*, *123*, 115–139.

Weidinger, J. T., Wang, J., & Ma, N. (2002). The earthquake-triggered rock avalanche of Cui Hua, Qin Ling Mountains, P. R. of China—The benefits of a lake-damming prehistoric natural disaster. *Quaternary International*, *93–94*, 207–214. https://doi.org/10.1016/s1040-6182(02)00019-8

Xing, A., Yuan, X., Xu, Q., Zhao, Q., Huang, H., & Cheng, Q. (2017). Characteristics and numerical runout modelling of a catastrophic rock avalanche triggered by the Wenchuan earthquake in the Wenjia valley, Mianzhu, Sichuan, China. *Landslides*, *14*(1), 83–98. https://doi.org/10.1007/s10346-016-0707-5

Yamada, M., Mangeney, A., Matsushi, Y., & Matsuzawa, T. (2018). Estimation of dynamic friction and movement history of large landslides. *Landslides*, *15*(10), 1963–1974. https://doi.org/10.1007/s10346-018-1002-4